Geophys. J. Int. (2002) **150,** 780–799

Elastic wave modelling in 3D heterogeneous media: 3D grid method

Zhang Jianfeng and Liu Tielin

Department of Engineering Mechanics, Dalian University of Technology, Dalian 116023, *China. E-mail: zjfhm@dlut.edu.cn*

Accepted 2002 April 4. Received 2002 March 21; in original form 2000 March 22

SUMMARY

We present a new numerical technique for elastic wave modelling in 3D heterogeneous media with surface topography, which is called the 3D grid method in this paper. This work is an extension of the 2D grid method that models *P-SV* wave propagation in 2D heterogeneous media. Similar to the finite-element method in the discretization of a numerical mesh, the proposed scheme is flexible in incorporating surface topography and curved interfaces; moreover it satisfies the free-surface boundary conditions of 3D topography naturally. The algorithm, developed from a parsimonious staggered-grid scheme, solves the problem using integral equilibrium around each node, instead of satisfying elastodynamic differential equations at each node as in the conventional finite-difference method. The computational cost and memory requirements for the proposed scheme are approximately the same as those used by the same order finite-difference method. In this paper, a mixed tetrahedral and parallelepiped grid method is presented; and the numerical dispersion and stability criteria on the tetrahedral grid method and parallelepiped grid method are discussed in detail. The proposed scheme is successfully tested against an analytical solution for the 3D Lamb problem and a solution of the boundary method for the diffraction of a hemispherical crater. Moreover, examples of surface-wave propagation in an elastic half-space with a semi-cylindrical trench on the surface and 3D plane-layered model are presented.

Key words: 3D grid method, 3D seismic modelling, 3D topography, elastic-wave theory, finite difference.

INTRODUCTION

Finite differences have proved their usefulness in modelling the propagation of elastic wave in heterogeneous media (Kelly *et al.* 1976; Virieux 1986), but the fact that they are implemented using regular grids gives rise to difficulties in incorporating surface topography and curved interfaces. As an alternative to the finite-difference method, one can use a finite-element method (Smith 1975) or finite-volume method (Dormy & Tarantola 1995). However, the finite-element method is computationally expensive and requires large amount of computer memory, especially in the 3D case; and the implementation of the free-surface boundary conditions deserves to be further studied for the finite-volume method even in the 2D case (Dormy & Tarantola 1995). In addition, the spectral element method (Komatitsch & Tromp 1999) is derived from the finite-element method to model 3D seismic wave propagation. Inclusion of topography at the free surface of an elastic medium leads to improved modelling of near-surface scattering effects, especially those in the high-frequency part of the wavefield; whereas modelling curved interfaces using a staircase approximation will produce artificial diffractions, especially for the high-order finite-difference schemes (Muir *et al.* 1992). Some efforts have been made to incorporate 3D surface topography into finite-difference and other numerical discretization methods. Tessmer & Kosloff (1994) handle the 3D surface topography by mapping a rectangular grid on to a curved grid based on a Chebychev spectral method; Ohminato & Chouet (1997) include 3D topography by discretizing the surface in a staircase and then setting the Lamé coefficients to zero on the free surface and in the atmosphere; and Hestholm & Ruud (1998) introduce the free-surface conditions of 3D topography by using a local rotated coordinated system at each point on the surface. However, tough and tedious efforts have to be paid to the implementation of the free-surface conditions for all the methods mentioned. Incidentally, the curved-grid approach (Tessmer & Kosloff 1994) is unstable for large surface curvature (Ohminato & Chouet 1997).

A numerical technique for modelling *P-SV*-wave propagation in 2D heterogeneous media, derived by incorporating the basic ideas of the finite-element (e.g. Smith 1975), finite-volume (e.g. Hirsch 1988) and staggered grid finite-difference (Virieux 1986) methods, has been put forward by Zhang & Liu (1999). There it was called the grid method to distinguish it from the finite-element or finite-volume methods. The method, with approximately the same memory requirements and computational cost as the second-order staggered grid scheme (Virieux 1986), is flexible in incorporating arbitrary surface topography, inner openings and irregular interfaces. Moreover, unlike the irregular grid

finite-difference scheme (Zhang 1997), the free-surface conditions of complex geometrical boundaries are satisfied naturally for this grid method. In this paper, we extend the grid scheme (Zhang & Liu 1999) from 2D to 3D heterogeneous structures. The resulting 3D grid method can accurately model the 3D topography and curved interfaces by using mixed tetrahedral and parallelepiped grids. Furthermore, no extra effort is needed for the 3D grid method satisfying the free-surface boundary conditions of 3D topography. Thus the inclusions of surface topography and curved interfaces in 3D elastic wave modelling become an easily task for the proposed numerical technique. Unlike the 2D grid method, the proposed 3D grid scheme adapts the parsimonious staggered-grid scheme of Luo & Schuster (1990). Only three displacements and three velocities need to be stored rather than three velocities and six stresses as in the conventional staggered-grid scheme (e.g. Virieux 1986) in each time step. The mixed tetrahedral and parallelepiped grids can reduce the number of the grid cells (similar to the elements in the finite-element method) in the numerical mesh in contrast with pure tetrahedral grids, so that the computational cost is reduced considerably by combining two kinds of grids. Hence a mixed tetrahedral and parallelepiped grid method is presented and discussed in detail here. Furthermore, the numerical dispersion analyses on the tetrahedral grid method and parallelepiped grid method are performed, respectively, and the stability criterion of the mixed tetrahedral and parallelepiped grid method is presented. The proposed scheme is tested against an analytical solution for the 3D Lamb problem to demonstrate the accuracy of this modelling algorithm. Moreover, the boundary method is used to benchmark the algorithm for a model with very steep surface topography. We also present examples of a 3D plane-layered model and surface-wave propagation in an elastic half-space with a semi-cylindrical trench on the surface.

BASIC THEORY

Parsimonious staggered-grid formulation

The algorithm is developed through adapting the parsimonious staggered-grid scheme. Unlike the parsimonious staggered-grid scheme of Luo & Schuster (1990), which employs three displacements of two time steps, we use the three displacements and three velocities in a staggered time level. Thus, the six stresses appear only as intermediate variables that do not need to be stored. The Parsimonious staggered-grid formulation that describes the elastic wave propagation in heterogeneous media can be expressed, using Cartesian coordinates, as

$$\tau_{ij} = \frac{1}{2} c_{ijkl} \left(\frac{\partial u_k}{\partial x_l} + \frac{\partial u_l}{\partial x_k} \right) \tag{1}$$

$$\rho \frac{\partial v_i}{\partial t} = \frac{\partial \tau_{ij}}{\partial x_j} \tag{2}$$

$$\frac{\partial u_i}{\partial t} = v_i \tag{3}$$

where $i, j, k, l = 1, \ldots, 3$, we assume the summation convention for repeated indices; and τ_{ij} are the Cartesian components of the stress tensor, u_i are the components of the particle displacement, v_i are the components of the particle velocity and c_{ijkl} are the components of the elastic stiffness tensor. The stiffness tensor c_{ijkl} may contain up to 21 independent parameters in the 3D case, but for an isotropic medium, two Lamé parameters λ and μ are enough to determine the stiffness tensor:

$$c_{ijkl} = \lambda \delta_{ij} \delta_{kl} + \mu (\delta_{ik} \delta_{jl} + \delta_{il} \delta_{jk}). \tag{4}$$

The proposed scheme employs a staggered grid in time. The displacements are defined at integral times and the velocities are defined at half times. Eq. (1) is used to obtain stresses from the known displacements at integral times; eq. (2) is employed in obtaining velocities at half times from the stresses (that will not appear in the following computations); and from eq. (3) we can solve displacements at the next integral time. Thus, the displacement field and the velocity field are updated. Hence, for the 3D case, only three displacements and three velocities, rather than six stresses and three velocities as in the conventional staggered-grid scheme, need to be stored for the proposed parsimonious staggered-grid scheme. In the following, we will discuss the spatial discretizations of eqs (1) and (2).

Weak form of equilibrium equations

The key to the proposed method is in transforming the differential equilibrium eqs (2) into a weak form of equilibrium equations (integral equilibrium equations) around each node, expressed in algebraic form. The scheme is based on a 3D discretization mesh of tetrahedrons and parallelepipedons. A local mesh around an inner node P (which is constructed by all the tetrahedrons and parallelepipedons that have a common node P) is shown in Fig. 1(a), where the tetrahedrons and parallelepipedons are called the grids, a basic cell of the proposed scheme. The three displacement components and the three velocity components are both defined at the nodes of the grids, and the six stress components (as intermediate variables) are defined at the centres of the grids. In the following, node P in Fig. 1 is considered in detail. For each tetrahedral grid, we link the centre of the tetrahedron and the centres of the facets and the midpoints of the edges to form a spatial folded surface, represented by the fine line in Fig. 1(b), which cuts a quarter of the volume of the tetrahedron; and for each parallelepiped grid, we link the centre of the parallelepipedon and the centres of the facets and the midpoints of the edges to form a spatial folded surface, represented by the fine line in Fig. 1(c), which cuts an eighth of the volume of the parallelepipedon. Thus all spatial folded surfaces, as those drawn by the fine lines in Figs 1(b) and (c), form a polyhedron V surrounding the node P.

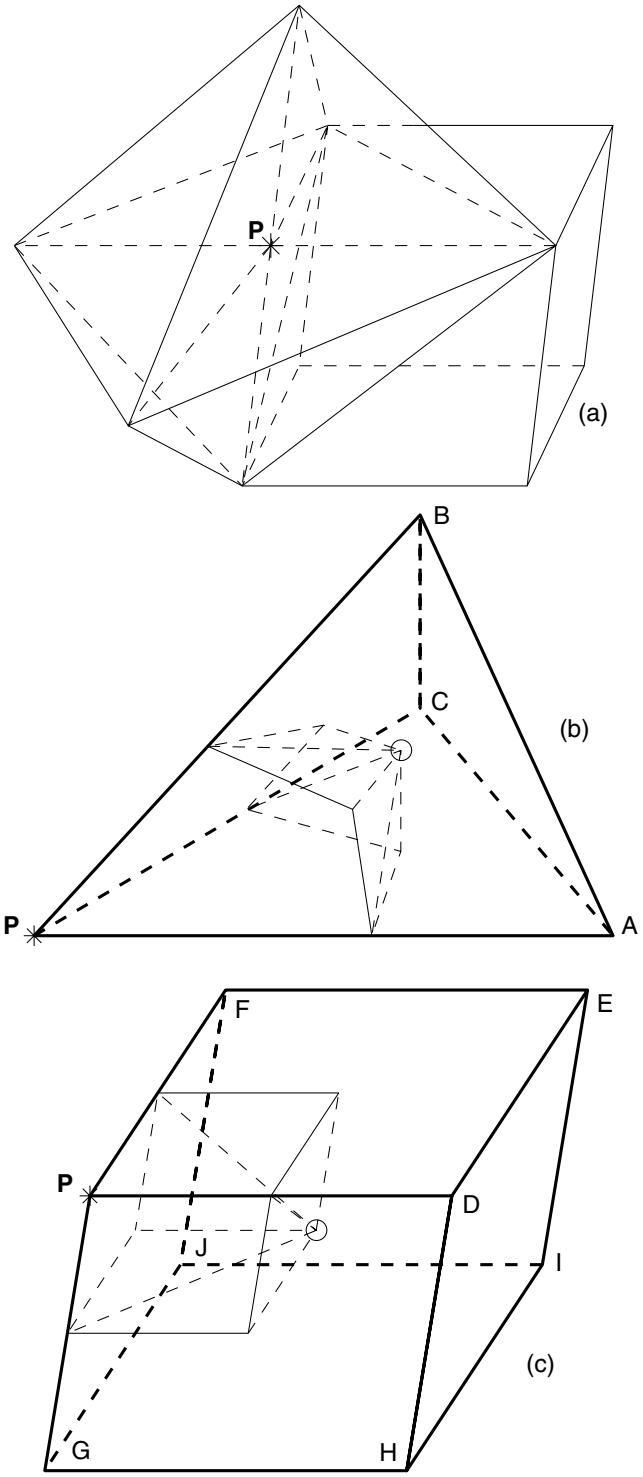

Figure 1. Local mesh for the inner node *P*. Part (a) is a local mesh around node *P*, which is constructed by all the tetrahedrons and parallelepipedons that have a common node *P*, (b) is a typical tetrahedral grid and (c) is a typical parallelepiped grid. The velocity and displacement components are defined at the nodes of the grids, as nodes *P*, *A*, etc. shown in (b) and (c). The stress components (as intermediate variables) are defined at the centres of the grids, represented by circles in (b) and (c).

Following Zhang & Liu (1999), we integrate both sides of eq. (2) over the volume inside the polyhedron V. This results in

$$\iiint_V \rho \frac{\partial v_i}{\partial t}\, dV = \oiint_S \left(\sum_{j=1}^{3} \tau_{ij} n_j \right) ds \tag{5}$$

where n_j are the direction cosines of the outward-directed normals to the facets of the polyhedron. By applying the lumped mass model to the discretization system, that is to say lumping the mass of the volume inside each grid (tetrahedron or parallelepipedon) to its nodes and

setting the density ρ to be zero in the inner domain of the grid, the volume integrals on the left-hand side of eq. (5) reduce to $M_P(\partial v_i/\partial t)_P$. Here $(\partial v_i/\partial t)_P$ is the time derivative of the velocity v_i at node P, and $M_P = M_P^t/4 + M_P^p/8$, where M_P^t and M_P^p are the sums of masses of the tetrahedral and parallelepiped grids around node P, respectively. Through introducing the assumption that the stresses are homogeneous inside each grid, we can rewrite the surface integrals on the right-hand side of eq. (5) as

$$\oiint_S \left(\sum_{j=1}^{3} \tau_{ij} n_j\right) ds = \sum_{l=1}^{m_t} \sum_{j=1}^{3} \tau_{ij}^l \iint_{S_t^l} n_j^l \, ds + \sum_{l=1}^{m_p} \sum_{j=1}^{3} \tau_{ij}^l \iint_{S_p^l} n_j^l \, ds \tag{6}$$

where m_t denotes the number of the tetrahedral grids around node P, m_p the number of the parallelepiped grids around node P, S_t^l the spatial folded surface inside the lth tetrahedral grid (as the fine solid line and dashed line shown in Fig. 1b), and S_p^l the spatial folded surface inside the lth parallelepiped grid (as the fine solid line and dashed line shown in Fig. 1c); τ_{ij}^l is the stress inside the lth tetrahedral or parallelepiped grid and n_j^l is the direction cosine of the outward-directed normals to the surface S_t^l or S_p^l. Eq. (6) shows that the calculations of the surface integrals on the right-hand side of eq. (5) can be obtained by accumulating the contributions of each grid. It is noted that the same approach has been followed by the finite-volume method (Dormy & Tarantola 1995). However, they approximated the volume integrals on the left-hand side of eq. (5) as a product of the volume inside the polyhedron V and the function values at node P, and then directly evaluated the surface integrals on the right-hand side of eq. (5) with a numerical quadrature formula, which actually yielded an irregular grid finite-difference discretized version of eq. (5).

For the lth tetrahedral grid, such as *PABC* shown in Fig. 1(b), the surface integral $\iint_{S_t^l} n_j^l \, ds$ denotes the projection of the area vector of surface S_t^l in the x_j direction, the value of which is related to the projected area of the facet *ABC* of the tetrahedron in the x_j direction. With $(c_j^P)_l$ denoting the lth surface integral $\iint_{S_t^l} n_j^l \, ds$ for $j = 1, 2, 3$, we have

$$\left(c_1^P\right)_l = \frac{1}{6}\begin{vmatrix} 1 & x_2^A & x_3^A \\ 1 & x_2^B & x_3^B \\ 1 & x_2^C & x_3^C \end{vmatrix}, \quad \left(c_2^P\right)_l = \frac{1}{6}\begin{vmatrix} x_1^A & 1 & x_3^A \\ x_1^B & 1 & x_3^B \\ x_1^C & 1 & x_3^C \end{vmatrix}, \quad \left(c_3^P\right)_l = \frac{1}{6}\begin{vmatrix} x_1^A & x_2^A & 1 \\ x_1^B & x_2^B & 1 \\ x_1^C & x_2^C & 1 \end{vmatrix}, \tag{7}$$

where x_j^A, x_j^B and x_j^C, for $j = 1, 2, 3$, are the three coordinates of nodes A, B and C. Moreover, for other three nodes A, B and C, we can achieve the analogous surface integrals, $(c_j^A)_l$, etc., by cyclic interchange of the superscripts in the order $P \to A \to B \to C \to P$ (see Fig. 1b); however, $(c_j^A)_l$ and $(c_j^C)_l$ should take the inverse values of the results of eq. (7). For the lth parallelepiped grid, such as *PDEFGHIJ* shown in Fig. 1(c), the surface integral $\iint_{S_p^l} n_j^l \, ds$ denotes the projection of the area vector of surface S_p^l in the x_j direction, the value of which is related to the projected area of the plane *GDF* of the parallelepipedon in the x_j direction. With $(e_j^P)_l$ denoting the lth surface integral $\iint_{S_p^l} n_j^l \, ds$ for $j = 1, 2, 3$, we have

$$\left(e_1^P\right)_l = -\frac{1}{4}\begin{vmatrix} 1 & x_2^G & x_3^G \\ 1 & x_2^D & x_3^D \\ 1 & x_2^F & x_3^F \end{vmatrix}, \quad \left(e_2^P\right)_l = -\frac{1}{4}\begin{vmatrix} x_1^G & 1 & x_3^G \\ x_1^D & 1 & x_3^D \\ x_1^F & 1 & x_3^F \end{vmatrix}, \quad \left(e_3^P\right)_l = -\frac{1}{4}\begin{vmatrix} x_1^G & x_2^G & 1 \\ x_1^D & x_2^D & 1 \\ x_1^F & x_2^F & 1 \end{vmatrix} \tag{8}$$

where x_j^G, x_j^D and x_j^F, for $j = 1, 2, 3$, are the three coordinates of nodes G, D and F. Moreover, for nodes D, E and F we can achieve $(e_j^D)_l$, $(e_j^E)_l$ and $(e_j^F)_l$ by replacing nodes (G, D, F) with nodes (H, E, P), (F, D, I) or (P, E, J); and we have $(e_j^P)_l = -(e_j^I)_l$, $(e_j^D)_l = -(e_j^J)_l$, $(e_j^E)_l = -(e_j^G)_l$ and $(e_j^F)_l = -(e_j^H)_l$ (see Fig. 1c).

Based on above discussions on the lumped mass model and the contributions of each grid to the surface integrals, we can obtain a weak form of equilibrium equations around node P (i.e. integral equilibrium equations) as

$$M_P\left(\partial v_i/\partial t\right)_P = \sum_{l=1}^{m_t} \sum_{j=1}^{3} \tau_{ij}^l \left(c_j^P\right)_l + \sum_{l=1}^{m_p} \sum_{j=1}^{3} \tau_{ij}^l \left(e_j^P\right)_l . \tag{9}$$

Spatial derivative formulae within the grids

Owing to the fact that the displacements are defined at the nodes of the tetrahedral and parallelepiped grids (i.e. an irregular mesh), we need to introduce irregular finite-difference operators to compute the spatial derivatives of displacement components in eq. (1). For a typical tetrahedral grid *PABC* (see Fig. 1b), the first-order spatial derivatives of the displacements inside the tetrahedron can be obtained from the linear tetrahedral element (Zienkiewicz & Taylor 1989) as

$$\frac{\partial u_i}{\partial x_j} = -\frac{1}{V}\left(c_j^P u_i^P + c_j^A u_i^A + c_j^B u_i^B + c_j^C u_i^C\right), \tag{10}$$

where c_j^P, etc. are same as $(c_j^P)_l$, etc. expressed in eq. (7), and u_i^P, etc. denote the ith displacement component at nodes P, etc.; V denotes the volume of the tetrahedron, and we have

$$V = \frac{1}{6}\begin{vmatrix} 1 & x_1^P & x_2^P & x_3^P \\ 1 & x_1^A & x_2^A & x_3^A \\ 1 & x_1^B & x_2^B & x_3^B \\ 1 & x_1^C & x_2^C & x_3^C \end{vmatrix}.$$

From eq. (10) we find the assumption that the stresses are homogeneous inside each grid to be valid for the tetrahedral grids. For the parallelepiped grids, we assume the stresses at the centres of the grids to represent the homogeneous stresses inside the parallelepiped grids. Thus only first-order spatial derivatives of the displacements at the centres of the grids need to be evaluated. For a typical parallelepiped grid *PDEFGHIJ* (see Fig. 1c), the first-order spatial derivatives of the displacements at its centre can be obtained using a 3D eight-node isoparametric element formula (by setting the three local coordinates to zero) as (Zienkiewicz & Taylor 1989)

$$\frac{\partial u_i}{\partial x_j} = -\frac{1}{W}\left(e_j^P u_i^P + e_j^D u_i^D + e_j^E u_i^E + e_j^F u_i^F + e_j^G u_i^G + e_j^H u_i^H + e_j^I u_i^I + e_j^J u_i^J\right), \tag{11}$$

where e_j^P, etc. are same as $(e_j^P)_l$, etc. expressed in eq. (8), u_i^P, etc. denote the ith displacement component at nodes P, etc., and W denotes the volume of the parallelepipedon.

Numerical implementations and memory requirements

Calculating $\partial u_i/\partial x_j$ for $i, j = 1, \ldots, 3$ in each grid using u_i by eqs (10) or (11) at time t, and then substituting them into eq. (1), we obtain the stresses τ_{ij} inside each grid at time t. Substituting stresses into the weak form of equilibrium equations of (9), we solve time derivatives of the velocities at each node, such as $(\partial v_i/\partial t)_P$. Then velocities of all nodes at time $t + \Delta t/2$ can be obtained using time integration. Furthermore, the displacements of all nodes at time $t + \Delta t$ can be solved using time integration by eq. (3). Thus the displacement field is updated from time level t to time level $t + \Delta t$, and the velocity field is updated from time level $t - \Delta t/2$ to time level $t + \Delta t/2$.

In the practical computations, the summations of the right-hand terms of eq. (9) are completed by looping all grids instead of summing all grids around each individual node. The following is a detailed description:

(i) computer memory units are assigned to all nodes of the discretization system;

(ii) for a tetrahedral grid, such as *PABC*, compute (for $i = 1, 2, 3$)

$$f_i^P = \sum_{j=1}^{3}\tau_{ij}c_j^P, \quad f_i^A = \sum_{j=1}^{3}\tau_{ij}c_j^A, \quad f_i^B = \sum_{j=1}^{3}\tau_{ij}c_j^B, \quad f_i^C = \sum_{j=1}^{3}\tau_{ij}c_j^C \tag{12}$$

(iii) for a parallelepiped grid, such as *PDEFGHIJ*, compute (for $i = 1, 2, 3$)

$$f_i^P = \sum_{j=1}^{3}\tau_{ij}e_j^P, \quad f_i^D = \sum_{j=1}^{3}\tau_{ij}e_j^D, \quad f_i^E = \sum_{j=1}^{3}\tau_{ij}e_j^E, \quad f_i^F = \sum_{j=1}^{3}\tau_{ij}e_j^F, \quad f_i^G = -f_i^E, \quad f_i^H = -f_i^F, \quad f_i^I = -f_i^P, \quad f_i^J = -f_i^D \tag{13}$$

(iv) adding the results of eqs (12) and (13) to the memory units corresponding to nodes P, A, B and C or P, D, E, F, G, H, I and J, respectively.

Thus we can complete the summations of the right-hand terms of eq. (9) by looping all grids once. In eqs (12) and (13) τ_{ij} are the stresses inside each grid and c_j^P, etc. and e_j^P, etc. are the geometric coefficients of each grid, which are same as $(c_j^P)_l$, etc. and $(e_j^P)_l$, etc. expressed in eqs (7) and (8).

It is noted from eqs (10) and (12) and eqs (11) and (13) that only the volumes and 12 geometric coefficients c_j^P, etc. or e_j^P, etc. are demanded in the computations for tetrahedral or parallelepiped grids, and the same coefficients c_j^P, etc. or e_j^P, etc. are used in both processes of obtaining stresses from displacements (eqs 10 or 11) and obtaining velocities from stresses (eqs 12 or 13). Hence, we only need to store a group of geometric coefficients for many grids that are congruent. Here all congruent grids are called one type of grid. If we limit the number of different types of grids in generating the numerical mesh, the memory requirements for the geometrical coefficients will become very low. Owing to the facts that we do not need to store coordinates for all nodes, and that other memory requirements, such as three displacements and three velocities in one time step of all nodes, are the same as in the conventional parsimonious staggered-grid scheme, we can thus declare that memory requirements for the proposed scheme are approximately the same as those used by the same order regular-grid finite-difference method. Moreover, only a single mesh, instead of two dual lattices as used in irregular grid finite-difference schemes (Dormy & Tarantola 1995; Zhang 1997), is needed for the numerical implementations of the proposed scheme. From the comparisons of eq. (10) with eq. (11) and eq. (12) with eq. (13) and bearing in the mind that the geometric coefficients of the parallelepiped grids have some kind of symmetry, we can conclude that the computational cost for the parallelepiped grids is the same as that for the tetrahedral grids. Since the mixed tetrahedral and parallelepiped grids can use fewer grid cells in the discretization of a same volume in contrast with pure tetrahedral grids, the computational cost needed by the mixed tetrahedral and parallelepiped grid method will be much less than that needed by the tetrahedral grid method.

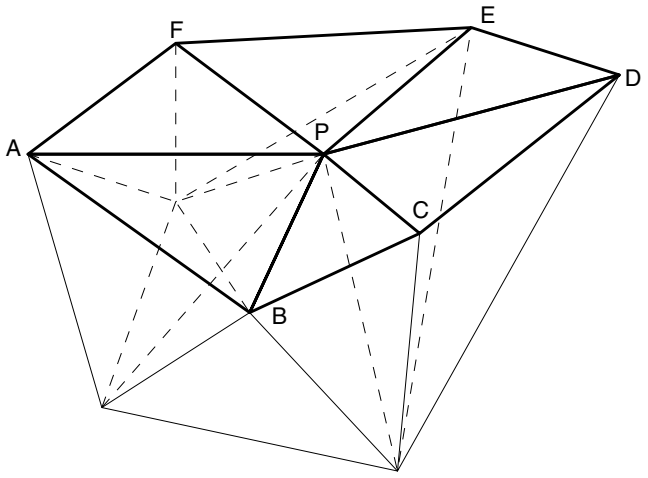

Figure 2. Local mesh for the surface node *P*. The *ABCDEFP* denotes the surface topography, represented by the black line. The figure is constructed by all the tetrahedrons that have a common node *P*.

BOUNDARY CONDITIONS

Only two types of boundary conditions have to be considered for modelling seismic wave propagation in complex 3D heterogeneous structures: the free-surface conditions of surface topography and inner openings, and the radiation conditions for simulating a semi-infinite medium. The implementation of the free-surface conditions, especially in the presence of 3D surface topography, is difficult for the conventional finite-difference method. However, following Zhang & Liu (1999), the proposed scheme presents a new approach for handling the free-surface conditions, which results in a natural implementation of free-surface boundary conditions for a 3D complex geometrical surface. Namely, the free-surface conditions are introduced by studying the equilibrium around a local domain in the vicinity of a surface, that is to extend the weak form of equilibrium equations of eq. (9) from internal to the boundaries.

It should be noted that the parallelepiped grid is not suitable for the discretization of the numerical mesh in the vicinity of a surface because of the assumption that the stresses are homogeneous inside the parallelepiped grids. Therefore, the numerical mesh just below a free surface is always constructed by the tetrahedral grids. A typical local mesh around a surface node is shown in Fig. 2, where the surface *ABCDEFP*, plotted by the black line, denotes the surface topography. Integrating both sides of eq. (2) over the volume surrounded by the polyhedron (which is constructed by all tetrahedrons that have a common node P), as the polyhedron shown in Fig. 2, leads to

$$\iiint_V \rho \frac{\partial v_i}{\partial t}\, dV = \iint_S \left(\sum_{j=1}^{3} \tau_{ij} n_j \right) ds + \iint_T \left(\sum_{j=1}^{3} \tau_{ij} n_j \right) ds, \tag{14}$$

where T is the surface topography, S is the outward surface of the polyhedron (to the exclusion of surface topography), and n_j are the direction cosines of the outward-directed normals to the facets of the polyhedron. Following the discussion on eq. (5), i.e. applying the lumped mass model to the discretization system and introducing the fact that the stresses are homogeneous inside each tetrahedral grid, we have

$$M_P(\partial v_i/\partial t)_P = \sum_{l=1}^{m_t} \sum_{j=1}^{3} \tau_{ij}^l \left(c_j^P\right)_l + \iint_T \left(\sum_{j=1}^{3} \tau_{ij} n_j \right) ds, \tag{15}$$

where $(\partial v_i/\partial t)_P$ is the time derivative of velocity v_i at node P, M_P is a quarter of the sum of the mass of all grids around node P, m_t is the number of the tetrahedral grids around node P, and τ_{ij}^l and $(c_j^P)_l$ have the same meaning as those used in eq. (9). Comparing the first terms of the right-hand side of eq. (15) with those in eq. (12), we find that these terms in eq. (15) have been obtained when looping all grids to compute the summations of the right-hand terms of eq. (9). Furthermore, the second terms on the right-hand side of eq. (15) are equivalent to the known total loads acting on the surface T in the x_j directions for $j = 1, 2, 3$ (which is the initial expression of the free-surface conditions). Adding all loads acting on the surface T to the memory units corresponding to node P in the process of looping the grids, we can solve the time derivatives of velocity components at node P from eq. (15). Hence, no extra effort is needed for the implementation of the free-surface conditions of complex geometrical boundaries.

For the radiation conditions, the problems arising for the proposed scheme are the same as for the conventional finite-difference schemes (e.g. Ohminato & Chouet 1997), and there is no special treatment needed. A transmission boundary condition based on a 1D characteristic analysis (Zhang & Liu 1997) is used here.

NUMERICAL ANALYSIS

We will perform a numerical analysis separately for the tetrahedral grid method and the parallelepiped grid method. For the parallelepiped grid method, we discuss a homogeneous grid case when the whole mesh is constructed using the same parallelepipedon. Here the parallelepipedon

is formed by distorting one facet (y–z plane) of a rectangular prism to making an angle θ with respect to the horizontal facet. For the tetrahedral grid method, we discuss a special inhomogeneous grid case when the whole mesh is constructed by different tetrahedrons. Here the tetrahedral grids are generated through splitting each right cube into five tetrahedrons of a regular orthogonal mesh. In the following, we will first discuss the dispersion relations, stability criterion and phase-velocity dispersion for the parallelepiped grid method, then those for the tetrahedral grid method are presented. Moreover, the stability of the free-surface conditions is studied, and the stability criterion for the mixed tetrahedral and parallelepiped grid method is proposed.

Dispersion relation and stability criterion for the parallelepiped grid method

The dispersion relation of the parallelepiped grid method is obtained as follows:

$$\sin^2\left(\frac{\omega\Delta t}{2}\right) = V^2\Delta t^2\left\{\frac{1}{\Delta x^2\Delta z^2\sin^2\theta}\cos^2(k_2/2)[\Delta z\sin(k_1/2)\cos(k_3/2) - \Delta x\cos\theta\cos(k_1/2)\sin(k_3/2)]^2 + \frac{1}{\Delta y^2}\cos^2(k_1/2)\sin^2(k_2/2)\cos^2(k_3/2) + \frac{1}{\Delta z^2}\cos^2(k_1/2)\cos^2(k_2/2)\sin^2(k_3/2)\right\} \tag{16}$$

where Δx, Δy and Δz denote the lengths of three sides of the parallelepiped grid, Δt is time sampling interval, ω the frequency, θ is the angle of one facet with respect to the horizontal facet, and $k_1 = (k_x\sin\theta + k_z\cos\theta)\Delta x$, $k_2 = k_y\Delta y$, $k_3 = k_z\Delta z$. Here k_x, k_y and k_z are the wavenumbers in the x, y and z directions, respectively. Eq. (16) denotes the P-wave dispersion relation when V is the P-wave velocity, and S-wave dispersion relation when V is the S-wave velocity. For details of the derivation of eq. (16) see Appendix A.

For stability we require $\sin^2(\omega\Delta t/2) \le 1.0$. From eq. (16) the stability criterion is given by

$$\alpha^2\Delta t^2\left\{\frac{1}{\Delta x^2\Delta z^2\sin^2\theta}\cos^2(k_2/2)[\Delta z\sin(k_1/2)\cos(k_3/2) - \Delta x\cos\theta\cos(k_1/2)\sin(k_3/2)]^2 + \frac{1}{\Delta y^2}\cos^2(k_1/2)\sin^2(k_2/2)\cos^2(k_3/2) + \frac{1}{\Delta z^2}\cos^2(k_1/2)\cos^2(k_2/2)\sin^2(k_3/2)\right\} \le 1.0, \tag{17}$$

where $\alpha = \sqrt{(\lambda+2\mu)/\rho}$ is the P-wave velocity. Let $\Delta x \ge \Delta z$ and $\Delta y \ge \Delta z$. The stability criterion of eq. (17) can be approximately reduced to

$$\Delta t \le \Delta z\sin\theta/\sqrt{3}\alpha. \tag{18}$$

From the stability criterion of eq. (18), it is seen that the stability of the parallelepiped grid method is independent of S-wave velocity and the Poisson ratio.

Phase-velocity dispersion of the parallelepiped grid method

Consider a plane wave with wavelength λ, for which the propagation direction has direction cosines T_1, T_2 and T_3. We have $k_x = (2\pi/\lambda)T_1$, $k_y = (2\pi/\lambda)T_2$ and $k_z = (2\pi/\lambda)T_3$. Let $\Delta x = \Delta y = \Delta z = h$. Following Virieux (1986), define the parameters $H = h/\lambda$ and $\gamma = \sqrt{2}\alpha\Delta t/h$. From eq. (16) the ratio of the phase velocity $\lambda\omega/2\pi$ to the true wave velocity are given by

$$q = \frac{\sqrt{2}}{\gamma H\pi\eta}\arcsin\left\{\frac{\gamma^2\eta^2}{2}\left[\frac{1}{\sin^2\theta}\cos^2(\pi HT_2)[\sin(\pi HT_n)\cos(\pi HT_3) - \cos\theta\cos(\pi HT_n)\sin(\pi HT_3)]^2 + \cos^2(\pi HT_n)\sin^2(\pi HT_2)\cos^2(\pi HT_3) + \cos^2(\pi HT_n)\cos^2(\pi HT_2)\sin^2(\pi HT_3)\right]\right\}^{1/2}, \tag{19}$$

where $T_n = T_1\sin\theta + T_3\cos\theta$, and q denotes the non-dimensional P-wave phase velocity (q_p) when $\eta = 1$ and the non-dimensional S-wave phase velocity (q_s) when $\eta = \sqrt{(1-2\upsilon)/2(1-\upsilon)}$. Here υ is the Poisson ratio. The function $q(H)$ shows, quantitatively, the phase-velocity dispersion arising from replacing the true partial differential equations with the finite-difference equations. For different H (H controls the number of nodes per wavelength), deviations of the quantities q_p and q_s from 1.0 show the degree of dispersion under this numerical mesh. Hence, the above dispersion analysis provides a rule to determine the spatial discretized size. For $\gamma = 0.8$ and $\theta = 60^\circ$, the P-wave phase-velocity dispersion curves, $q_p(H)$, are plotted in Fig. 3 for different propagation directions of the plane wave, which are $T_1 = 1.0$, $T_2 = 0.0$ and $T_3 = 0.0$, $T_1 = 1/\sqrt{2}$, $T_2 = 0.0$ and $T_3 = 1/\sqrt{2}$, and $T_1 = 1/\sqrt{3}$, $T_2 = 1/\sqrt{3}$ and $T_3 = 1/\sqrt{3}$. The figure is valid for any Poisson ratio. The quantity q_p is always lower than 1 and approaches 1 for small H. For $H \le 0.05$, $q_p \approx 1.0$. This means that the edges of the parallelepiped grids should be 1/20 of the wavelength in order to model the P wave accurately. For $\gamma = 0.8$ and $\theta = 60^\circ$, the S-wave phase-velocity dispersion curves, $q_s(H)$, are plotted in Fig. 4 for various Poisson ratios, where the Poisson ratios are $\upsilon = 0.25$, 0.499, and the direction cosines of the propagation directions of the plane wave are $T_1 = 1.0$, $T_2 = 0.0$ and $T_3 = 0.0$, $T_1 = 1/\sqrt{2}$, $T_2 = 0.0$ and $T_3 = 1/\sqrt{2}$, and $T_1 = 1/\sqrt{3}$, $T_2 = 1/\sqrt{3}$ and $T_3 = 1/\sqrt{3}$. For $H \le 0.05$, $q_s \approx 1.0$. This gives a same rule of thumb as for the P-wave modelling. Moreover, the behaviour of q_s does not degrade as υ goes to 0.5. This suggests that the parallelepiped grid method behaves correctly inside liquids, and at liquid–solid interfaces.

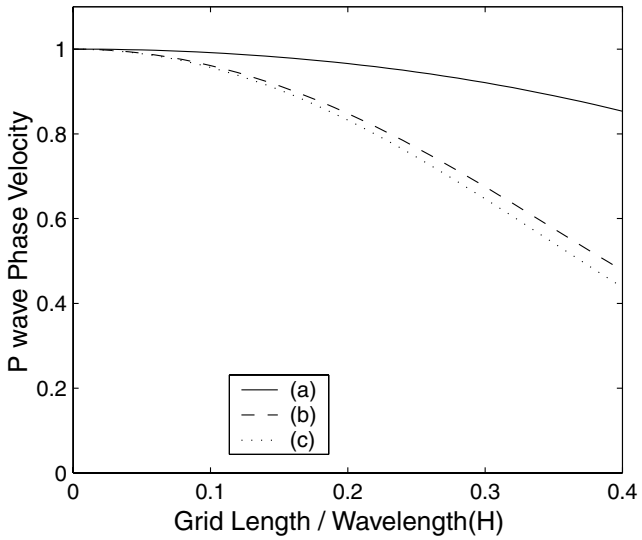

Figure 3. Dispersion curves of the parallelepiped grid method for non-dimensional *P*-wave phase velocity with the parameter $\gamma = 0.8$. Results for various propagation directions of the plane wave, that are: (a) $T_1 = 1.0$, $T_2 = 0.0$ and $T_3 = 0.0$, (b) $T_1 = 1/\sqrt{2}$, $T_2 = 0.0$ and $T_3 = 1/\sqrt{2}$, and (c) $T_1 = 1/\sqrt{3}$, $T_2 = 1/\sqrt{3}$ and $T_3 = 1/\sqrt{3}$. They are independent of the Poisson ratio.

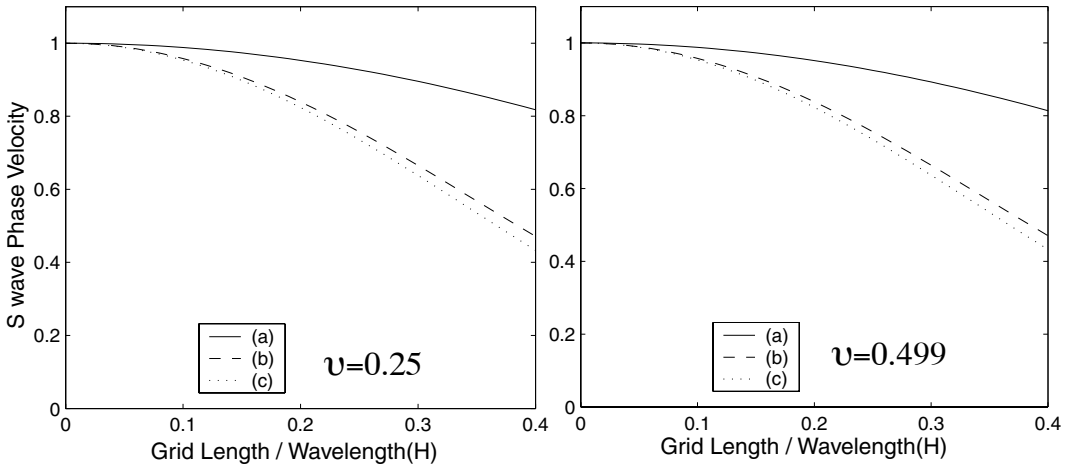

Figure 4. Dispersion curves of the parallelepiped grid method for a non-dimensional *S*-wave phase velocity with $\gamma = 0.8$. Results for various propagation directions of the plane wave: (a) $T_1 = 1.0$, $T_2 = 0.0$ and $T_3 = 0.0$, (b) $T_1 = 1/\sqrt{2}$, $T_2 = 0.0$ and $T_3 = 1/\sqrt{2}$, and (c) $T_1 = 1/\sqrt{3}$, $T_2 = 1/\sqrt{3}$ and $T_3 = 1/\sqrt{3}$, are shown on the same graph for different Poisson ratios.

Dispersion relations and stability criterion for the tetrahedral grid method

The dispersion relations of the tetrahedral grid method for a Poisson ratio of 0.25 are obtained in Appendix B. For a special case, that is $k_x = k_y = k_z = k$, we have a simple form as follows:

$$\frac{72h^2}{\Delta t^2 \alpha^2} \sin^2\left(\frac{\omega \Delta t}{2}\right) = 74 - 34\cos^2(kh) - 40\cos(kh) \tag{20}$$

$$\frac{24h^2}{\Delta t^2 \beta^2} \sin^2\left(\frac{\omega \Delta t}{2}\right) = 38 + 2\cos^2(kh) - 40\cos(kh), \tag{21}$$

where h is the interval of the regular orthogonal mesh, Δt is the time sampling interval, and $\alpha = \sqrt{(\lambda + 2\mu)/\rho}$ and $\beta = \sqrt{\mu/\rho}$ are the *P*- and *S*-wave velocities, respectively. Eq. (20) denotes the *P*-wave dispersion relation; and eq. (21) the *S*-wave dispersion relation. For stability we require that $\sin^2(\omega \Delta t/2) \leq 1.0$. From eqs (20) and (21) the stability criterion can be approximately given by

$$\Delta t \leq \sqrt{3} h / 2\alpha. \tag{22}$$

It is noted that the stability criterion of eq. (22) is only valid for the Poisson ratio $\upsilon = 0.25$. However, comparing eq. (22) with eq. (18) reveals that the stability criterion of the tetrahedral grid method is more relaxed than that of the parallelepiped grid method. Thus, for the mixed

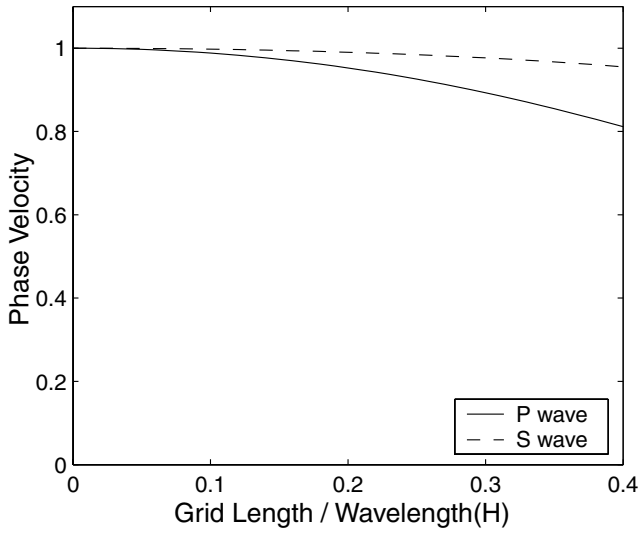

Figure 5. Dispersion curves of the tetrahedral grid method for non-dimensional *P*- and *S*-wave phase velocities with $\gamma = 0.8$. The propagation directions of the plane wave is $T_1 = 1/\sqrt{3}$, $T_2 = 1/\sqrt{3}$ and $T_3 = 1/\sqrt{3}$. The Poisson ratio is 0.25.

tetrahedral and parallelepiped grid method presented in this paper, eq. (18) can serve as a stability criterion to chose proper temporal and spatial discretized intervals.

Phase-velocity dispersion of the tetrahedral grid method

Following the discussion on the parallelepiped grid method, we can obtained phase-velocity dispersion curves $q_p(H)$ and $q_s(H)$ based on eqs (20) and (21), which are plotted in Fig. 5 for $\gamma = 0.8$, $\upsilon = 0.25$ and the propagation direction of $T_1 = 1/\sqrt{3}$, $T_2 = 1/\sqrt{3}$ and $T_3 = 1/\sqrt{3}$. It is found that $q_p \approx 1.0$ and $q_s \approx 1.0$ for $H \leq 0.09$ from Fig. 5. Hence, the rule of thumb, to determine the discretized size, for the parallelepiped grid method is more restrictive than that for the tetrahedral grid method. Thus, for the mixed tetrahedral and parallelepiped grid method presented in this paper, we can use the rule of thumb as for the parallelepiped grid method to determine the spatial discretized size.

Stability of free-surface conditions

It has been observed that instabilities occurring when solving hyperbolic equations are frequently caused by the treatment of the free-surface boundary conditions (Gottlieb *et al.* 1982; Kosloff *et al.* 1990). Hence, it is interesting to analyse the stability of the free-surface conditions satisfied naturally by the 3D grid method. We study a plane surface (parallel to the *x*–*y* plane) case when the tetrahedral grids are generated through splitting each right cube into five tetrahedrons of a regular orthogonal mesh. Following the discussion on the finite-difference equations for the tetrahedral grid method, we can achieve the finite-difference equations for the surface case (see Appendix C). Let a plane *P* wave vertically incident upon the free surface be $A\exp[-i(k_z z + \omega t)]$. The displacement components can be expressed as

$$u_1 = 0, \qquad u_2 = 0, \qquad u_3 = Ae^{-i(k_z z+\omega t)} + Ae^{i(k_z z-\omega t)}. \tag{23}$$

Calculating the displacement components at nodes from eq. (23) and then substituting them into the finite-difference equations of Appendix C, we obtain the dispersion relation for the local surface for a vertical incident *P* wave as follows:

$$\sin^2(\omega\Delta t/2) = (\alpha^2\Delta t^2/h^2)\sin^2(k_z h/2). \tag{24}$$

From eq. (24) we can approximately solve the stability criterion for the free-surface conditions as

$$\Delta t \leq h/\alpha. \tag{25}$$

The stability criterion in eq. (25) is more relaxed than that expressed in eq. (18) for the mixed tetrahedral and parallelepiped grid method, so that the stability of free-surface conditions can be guaranteed for the 3D grid method.

NUMERICAL SIMULATIONS

Analytic comparison

The accuracy of the proposed method is tested through a comparison of numerical results with an analytical solution of the 3D Lamb problem. The analytical solution is achieved by convolving the free-surface Green function (Pekeris 1955) with the source function. A vertical Gaussian

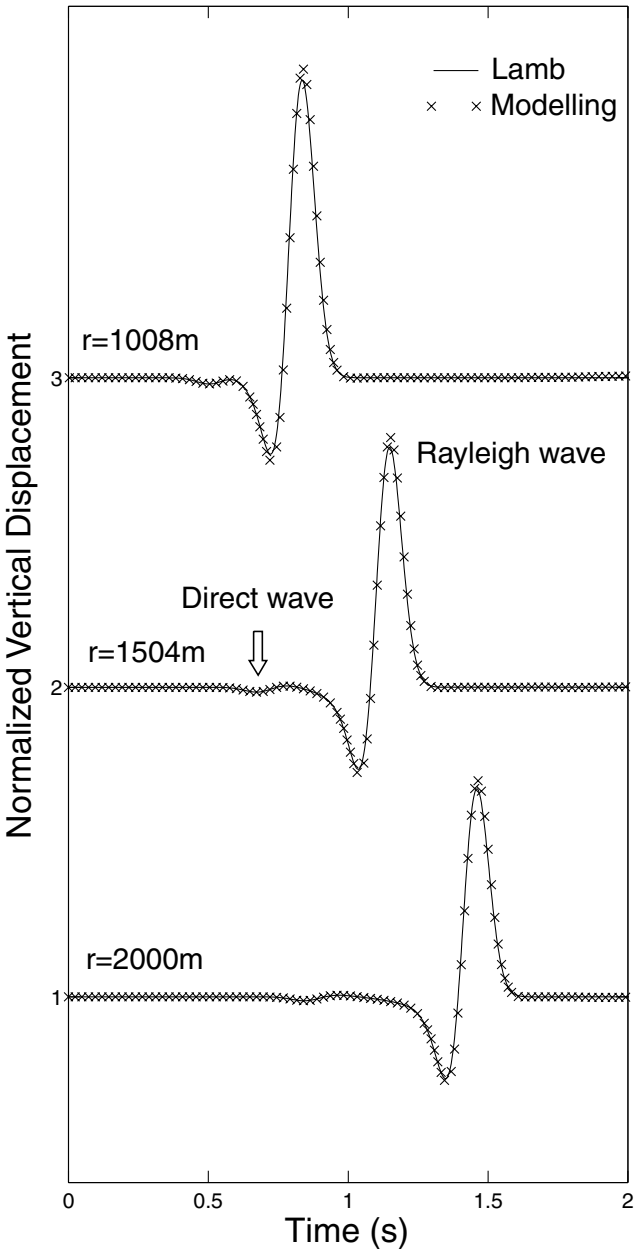

Figure 6. Comparison between numerical and analytical vertical components of the displacement for the 3D Lamb problem at various stations on the free surface. The display is for the edge length of grids of 16 m.

point source, with a maximum frequency of 10 Hz, is loaded at the free surface. Two numerical results, which differ in the discretization of the numerical mesh of the half-space, are illustrated in Figs 6 and 7. Fig. 6 shows a comparison of the vertical displacements at three stations, 1008, 1504 and 2000 m from the source, on the free surface. The numerical model for this results is made up of tetrahedral and parallelepiped grids with the edges of the tetrahedrons and parallelepipedons of 16 m, where the parallelepipedon is a distortion of a right cube with its one facet making an angle of 60° with respect to the horizontal facet and the tetrahedron is formed by splitting each of these parallelepipedons into six tetrahedrons. Fig. 7 shows a comparison of the vertical displacements for longer propagation paths at four stations, 1200, 1800, 2400 and 3000 m from the source, on the free surface. The numerical model for Fig. 7 is made up of tetrahedral and right cube grids with a minimum edge of 20 m, where the tetrahedral grids in the vicinity of the surface are generated through splitting each right cube into five tetrahedrons. This can be considered as one kind of inhomogeneous grid case. The computational cost of the result of Fig. 7 is reduced to a quarter by exploiting the symmetry of the model on *xy*- and *yz*-planes with *z*-axis pointing downward (which also represents another advantage of the proposed method, i.e. the symmetry condition can be implemented very easily). The receivers for the result of Fig. 7 are positioned at a line on the surface, which starts from the source point and make an angle of 45° with respect to the *x*-axis. The semi-finite medium has a *P*-wave velocity of 3000 m s^{-1} and an *S*-wave velocity of 1730 m s^{-1} for two numerical results. The grid edges are 1/19 of *P* wavelength and 1/11

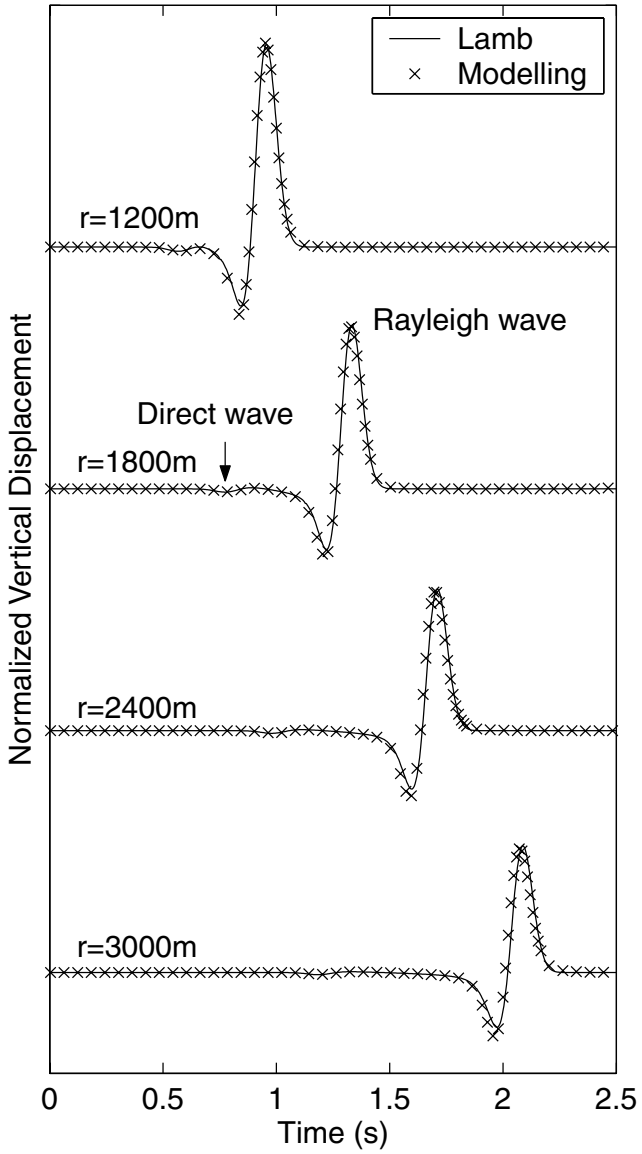

Figure 7. Comparison between numerical and analytical vertical components of the displacement at various stations on the free surface for longer propagation paths of the 3D Lamb problem. The display is for an inhomogeneous grid case with a minimum edge length of grids of 20 m.

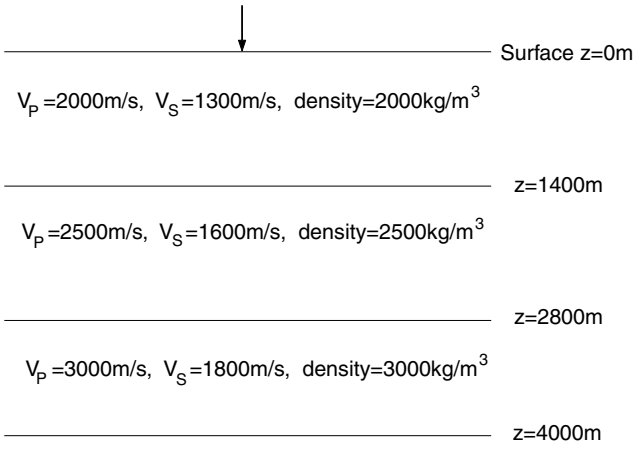

Figure 8. Plane-layered model with vertically increasing velocities and density.

of *S* wavelength for Fig. 6 and 1/15 of *P* wavelength and 1/9 of *S* wavelength for Fig. 7. From Figs 6 and 7 we find that the surface wave propagates without dispersion, and the discrepancy in amplitude between numerical and analytical Rayleigh waves is less than 5 per cent. The total propagation times are 2.0 s with a time step of 3 ms for Fig. 6 and 2.5 s with a time step of 4 ms for Fig. 7.

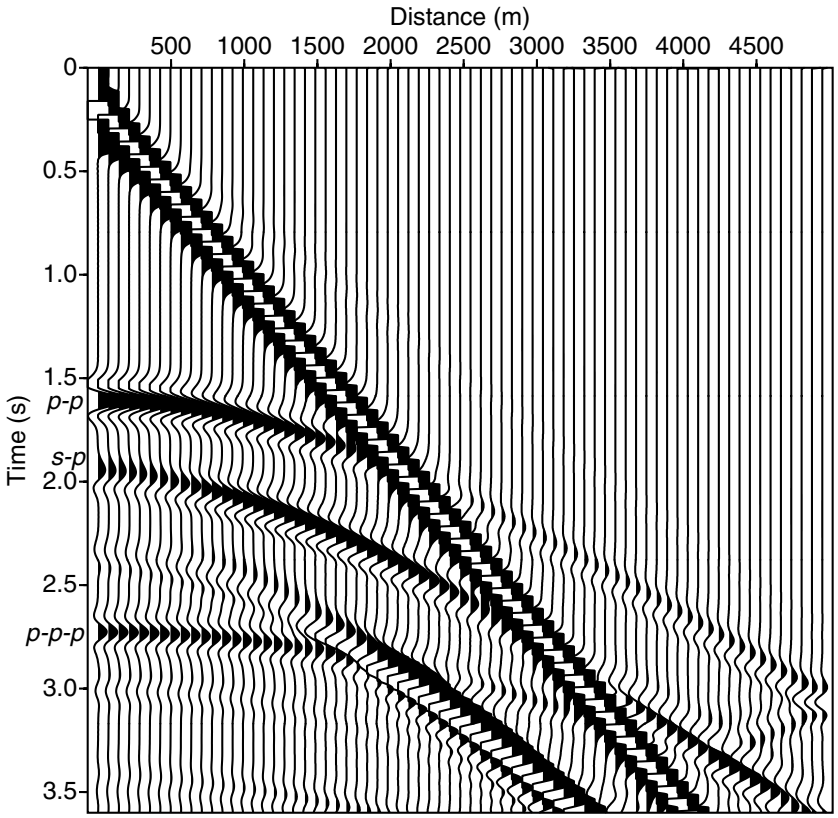

Figure 9. Numerical seismogram of vertical displacements at the free surface. The receivers are positioned at a line on the free surface, which starts from the source point and make an angle of 45° against *x*-axis. All amplitudes take their inverse values and the amplitudes of the direct and Rayleigh waves are reduced to 20 per cent.

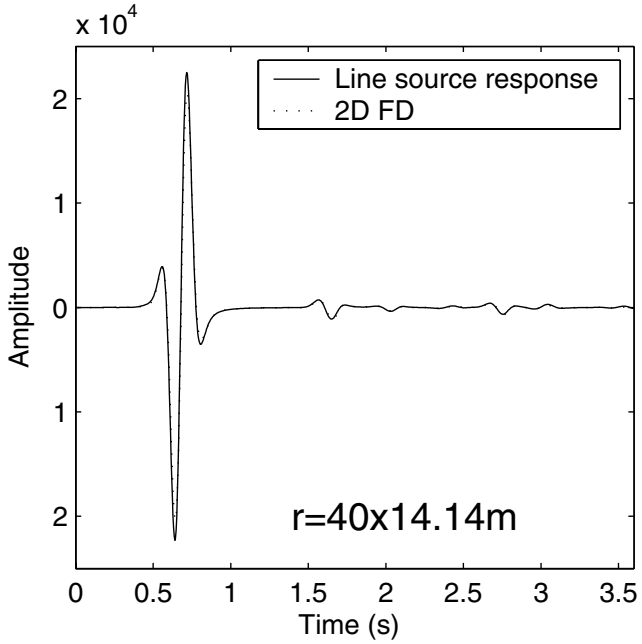

Figure 10. Comparison between the 2D finite-difference solution with the line-source response for the vertical displacement on the free surface at a source–receiver distance of 40 × 14.14 m. The line-source response is obtained from the superposition of the 3D point-source responses of Fig. 9.

Layered model

A synthetic seismogram is generated for a plane-layered model, as illustrated in Fig. 8, to assess the proposed algorithm in modelling elastic wave propagation in heterogeneous media. A vertical Ricker wavelet point source, with a maximum frequency of 15 Hz, is loaded at the free surface of the 3D layered model. Let the source point be $x = 0$, $y = 0$, $z = 0$, and the z-axis point vertical downward. The receivers with a spacing of 14.14 m are positioned at the line on the free surface, which starts from the source point and make an angle of 45° against x-axis. The numerical seismogram of vertical displacements is showed in Fig. 9, where all amplitudes take their inverse values and the amplitudes of the direct and Rayleigh waves are reduced to 20 per cent in order to show the reflected waves coming from the plane interfaces clearly. The reflected P waves coming from the first interface as a result of the incident P wave (P–P) and the incident S wave (S–P), and reflected P wave (P–P–P) coming from the second interface are seen clearly in Fig. 9. The practical computation is done on a quarter of the model by exploiting the symmetry, thus the computational cost is much reduced. The numerical model is made up of tetrahedral and parallelepiped grids with a minimum edge of 10 m. The time interval used is 2 ms.

To assess the accuracy of the proposed scheme, we transform the above point-source response into line-source responses by carrying out an integration along the receiver coordinate (Wapenaar *et al.* 1992), and then compare the resulting line-source responses with 2D

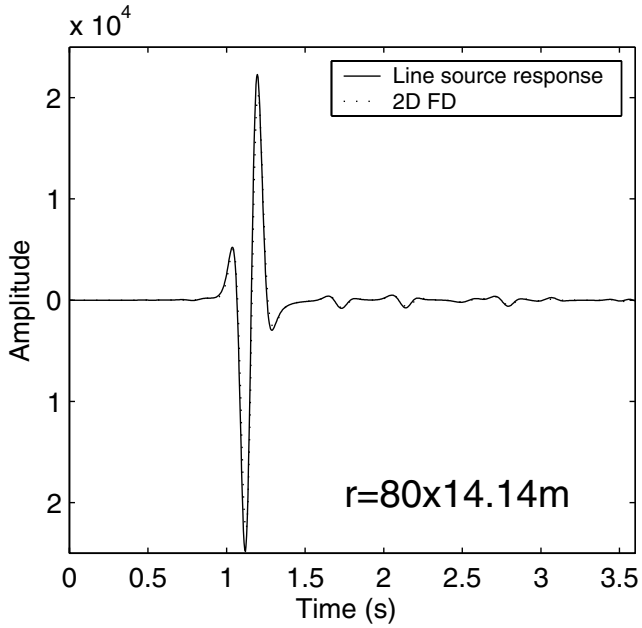

Figure 11. Comparison between the 2D finite-difference solution with the line-source response for the vertical displacement on the free surface at a source–receiver distance of 80 × 14.14 m. The line-source response is obtained from the superposition of the 3D point-source responses of Fig. 9.

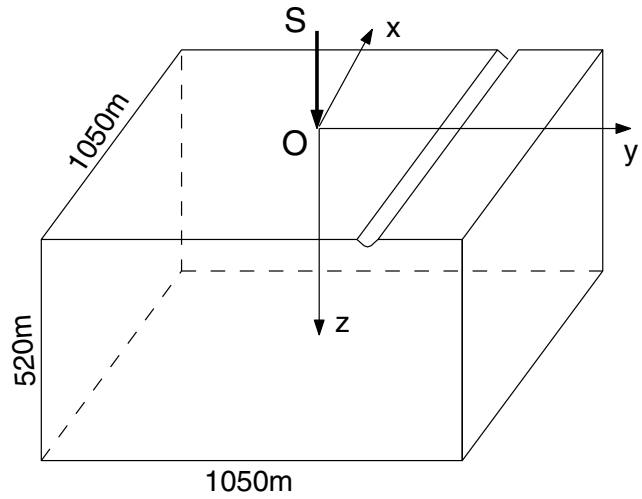

Figure 12. An elastic half-space with a semi-cylinder trench on the free surface. The source, shown by an arrow, is load at the centre point (O) on the surface. The normal distance between the source and the trench is 280 m. The semi-cylindrical trench has a radius of 14 m. The semi-finite medium has a P-wave velocity of 2000 m s^{-1} and an S-wave velocity of 1130 m s^{-1}.

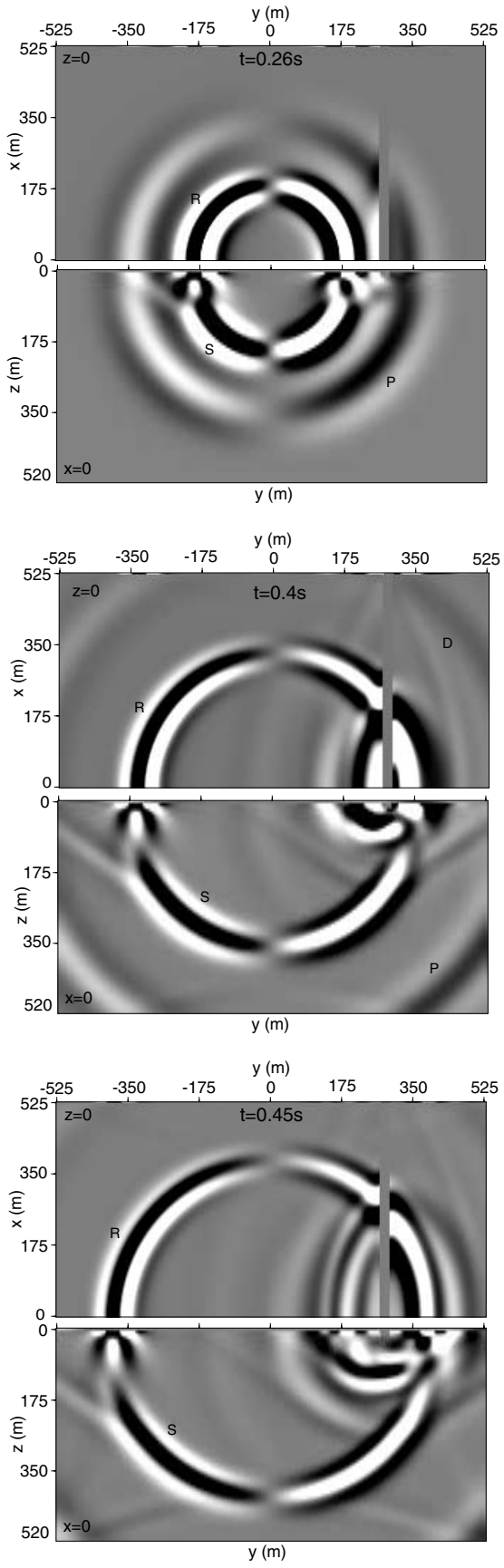

Figure 13. Snapshots of y-direction component of the displacement at propagation times of 0.26, 0.4 and 0.45 s. The top of each figure is related to the free surface, and the bottom is related to a vertical plane ($x = 0$) that is orthogonal with the trench on the surface. A vertical Ricker wavelet point source is positioned at the midpoint of the intersection line of two planes ($x = 0$, $y = 0$, $z = 0$). The trench can be seen in $z = 0$ surface at $y = 280$ m.

finite-difference modelling results. Figs 10 and 11 show the comparisons of vertical displacements at stations, 40×14.14 m and 80×14.14 m from the source, on the free surface. In spite of the errors derived from the transformation of the point-source response into the line-source one, two results agree well in Figs 10 and 11.

Trench on the surface

To test the quality of the proposed scheme in accounting for the surface topography, we present an example of elastic wave propagation in a semi-infinite medium with a semi-cylinder trench on the free surface. The model has a size of $1050 \times 1050 \times 520$ m^3 as shown in Fig. 12. The semi-cylindrical trench has a radius of 14 m, and it lies parallel to the x-direction. A vertical Ricker wavelet point source, with a maximum frequency of 35 Hz, is loaded at the free surface ($x = 0$, $y = 0$, $z = 0$), as indicated by an arrow in Fig. 12. The normal distance between the source and the trench is 280 m. The semi-finite medium has a P-wave velocity of 2000 m s^{-1} and an S-wave velocity of 1130 m s^{-1}. Based on the symmetry of the model on the yz-plane at $x = 0$, we can reduce the computational cost by using half of the model in practical computations. The numerical mesh is made up of tetrahedral and parallelepiped grids with a minimum edge of 3.5 m. The minimum grid edges are 1/16 the P wavelength and 1/9 the S wavelength. For details on the generation of complicated numerical mesh see Thompson *et al.* (1985). The computation, with 6 859 779 nodes, 2 614 950 tetrahedral grids and 6 300 000 parallelepiped grids, takes a CPU time of 340 min on a SUN Solaris Sparc II when performing 450 time steps of 1 ms.

Snapshots of the y-direction component of the displacement on the free surface ($z = 0$) and the vertical plane ($x = 0$) that is orthogonal with the trench at propagation times of 0.26, 0.4 and 0.45 s are shown in Fig. 13. The snapshots show very clear wave fronts of the Rayleigh surface wave, the direct P wave, the direct S wave, and reflected and diffracted waves caused by the trench. The conical wave can be found in the vertical plane ($x = 0$). Comparing the snapshots of the surface with that of the vertical plane illustrates the 'surface' characteristics of the Rayleigh wave. Owing to its shorter wavelength, the diffraction of the Rayleigh wave is much stronger than that of the P wave when propagating through the trench, as can be seen clearly in the snapshots.

Hemispherical crater

An example of elastic wave propagation in a hemispherical crater in a homogeneous half-space is used to test the accuracy of the proposed algorithm in the presence of 3D surface topography. Sanchez-Sesma (1983) studied the response of a hemispherical crater in a homogeneous

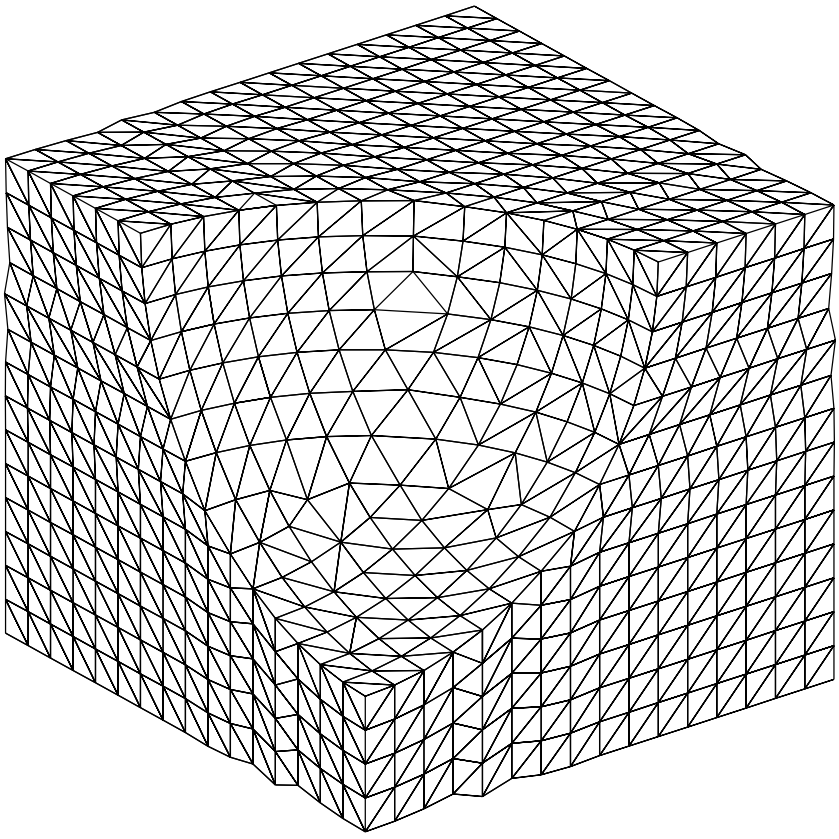

Figure 14. A local mesh in the vicinity of the crater for $\eta = 0.25$. The mesh is constructed by the tetrahedral grids.

half-space to a vertically incident plane *P* wave based on an approximate boundary method. He presented the amplitude of the displacement recorded at the surface of the crater for different normalized frequencies $\eta = 2a/\lambda_p$, where a denotes the radius of the crater and λ_p the wavelength of the incident *P* wave. His result is used here to test the algorithm quantitatively.

The semi-finite medium has a *P*-wave velocity of 3000 m s^{-1} and an *S*-wave velocity of 1730 m s^{-1}. The density is 2500 kg m^{-3}. The source is a vertically incident plane *P* wave, which is a Ricker wavelet in time with a peak frequency of 5 Hz. The radius of the hemispherical crater is 75 and 150 m for the normalized frequencies of 0.25 and 0.5, respectively. Transforming the seismograms for receivers at the surface into frequency domain and picking the amplitudes corresponding to 5 Hz, we can then compare the results with Sanchez-Sesma (1983).

The mesh is made up of tetrahedral grids in the vicinity of the surface and right cube grids below those. Again the symmetry of the model on *xy*- and *yz*-planes with the *z*-axis pointing downward is exploited to reduce the computational cost. Fig. 14 shows a local mesh in the vicinity of the crater for $\eta = 0.25$. It can be seen that the mesh accurately models the 3D surface topography. Normally the number of points per wavelength is less for higher-order schemes. However, for the correct description of the geometry of the hemisphere, small mesh spacing is required even for higher-order schemes (e.g. Komatitsch & Tromp 1999). From Fig. 14 we can again find the flexibility of the proposed tetrahedral and parallelepiped grid scheme, i.e. no much extra points are needed for including surface topography and the edge of grids are more or less constant.

Fig. 15 shows the results of the proposed grid scheme for $\eta = 0.25$ and 0.5. The corresponding results of Sanchez-Sesma can be seen in Fig. 15 of Komatitsch & Tromp (1999). It is found through comparing the two figures that the agreement is excellent. In particular, the strong amplification close to the edges of the crater is reproduced well. Note that the amplification level of the vertical component reaches a very high value in the centre for $\eta = 0.5$ (which is 2 for the plane surface).

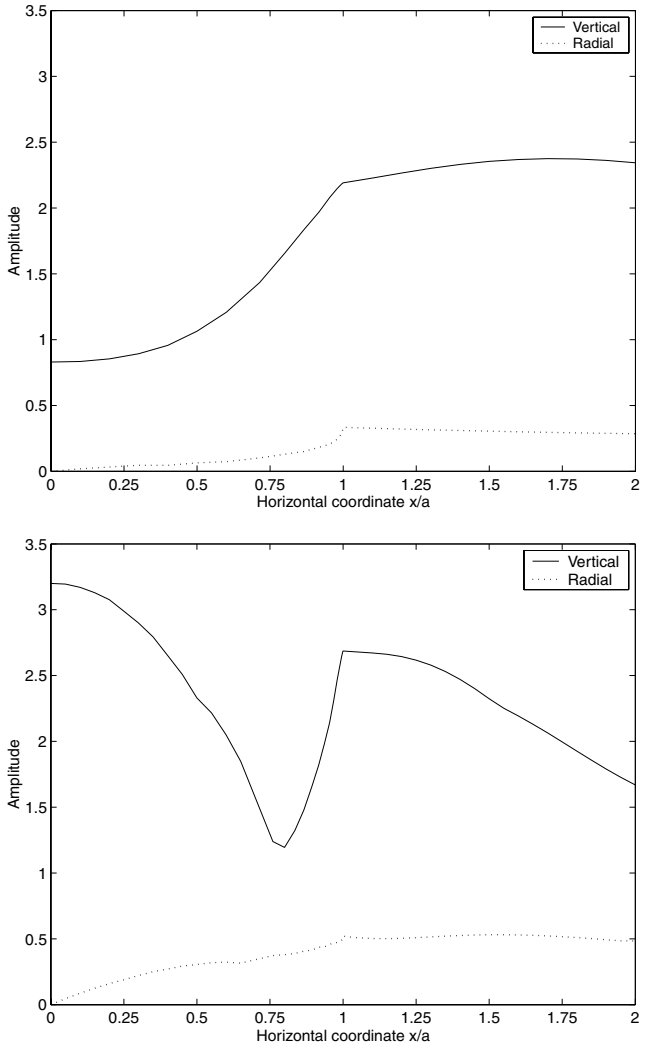

Figure 15. Amplitudes of the two components of displacement recorded along the crater, from $x/a = 0$ (centre of the crater) to $x/a = 2$. The vertical and radial components are displayed. The results are shown for two normalized frequency $\eta = 0.25$ (top) and $\eta = 0.5$ (bottom).

CONCLUSIONS

We have presented a new numerical modelling algorithm for elastic wave propagation in 3D heterogeneous media. The scheme is an extension of the 2D grid method. The algorithm can accurately model the surface topography, inner openings and curved interfaces by using an unstructured mesh. The mesh used is similar to the mesh generated for the finite-element method, thus many available mesh generation algorithms can be applied for the scheme. Moreover, no extra effort is needed for the scheme to satisfy the free-surface boundary conditions of 3D topography. The computational cost and memory requirements for the algorithm are approximately the same as those used by a same order regular-grid finite-difference method. The properties outlined above allow the proposed scheme to easily solve the difficulties, such as the inclusion of 3D surface topography, that arise for the standard finite-difference schemes. Comparisons with an analytic solution of the 3D Lamb problem and a solution of the boundary method for the diffraction of a hemispherical crater and a 3D layered model show the new scheme to be highly accurate, and the numerical simulation on wave propagation in a half-space with a corrugated surface demonstrates its high quality. The scheme can serve as a powerful tool for the study of wave propagation phenomena in the vicinity of non-planar surface and interfaces of complicated 3D heterogeneous structures.

ACKNOWLEDGMENTS

We are grateful to the Education Ministry of China and the National Natural Science Fund for Distinguished Young Scholars of China who supported this work. We thank Jeroen Tromp and an anonymous reviewer for constructive comments that improved the manuscript.

REFERENCES

Dormy, E. & Tarantola, A., 1995. Numerical simulation of elastic wave propagation using a finite volume method, *J. geophys. Res.,* **100**, B2, 2123–2133.

Gottlieb, D., Gunzburger, M. & Turkel, E., 1982. On numerical boundary treatment of hyperbolic systems for finite difference and finite element methods, *SIAM J. Num. Anal.,* **19**, 671–682.

Hestholm, S.O. & Ruud, B.O., 1998. 3D finite-difference elastic wave modeling including surface topography, *Geophysics,* **63**, 613–622.

Komatitsch, D. & Tromp, J., 1999. Introduction to the spectral element method for three-dimensional seismic wave propagation, *Geophys. J. Int.,* **139**, 806–822.

Kosloff, D., Kessler, D., Filho, A.Q., Tessmer, E., Behle, A. & Strahilevitz, R., 1990. Solution of the equations of dynamic elasticity by a Chebyshev spectral method, *Geophysics,* **55**, 734–748.

Hirsch, C., 1988. *Numerical Computation of Internal and External Flows,* Wiley, New York

Kelly, K.R., Ward, R.W., Treitel, S. & Alford, R.M., 1976. Synthetic seismograms: a finite-difference approach, *Geophysics,* **41**, 2–27.

Luo, Y. & Schuster, G., 1990. Parsimonious staggered grid finite-differencing of the wave equation, *Geophys. Res. Lett.,* **17**, 155–158.

Muir, F., Dellinger, J., Etgen, J. & Nichols, D., 1992. Modeling elastic fields across irregular boundaries, *Geophysics,* **57**, 1189–1193.

Ohminato, T. & Chouet, B., 1997. A free-surface boundary condition for including 3D topography in the finite-difference method, *Bull. seism. Soc. Am.,* **87**, 494–515.

Pekeris, C.L., 1955. The seismic surface pulse, *Proc. Nat. Acad. Sci.,* **41**, 469–480.

Sanchez-Sesma, F.J., 1983. Diffraction of elastic waves by three-dimensional surface irregularities, *Bull. seism. Soc. Am.,* **73**, 1621–1638.

Smith, W.D., 1975. The application of finite-element analysis to body wave propagation problems, *Geophys. J. R. astr. Soc.,* **42**, 747–768.

Tessmer, E. & Kosloff, D., 1994. 3D elastic modeling with surface topography by a Chebyshev spectral method, *Geophysics,* **59**, 464–473.

Thompson, J.F., Warsi, Z.U.A. & Mastin, C.W., 1985. *Numerical Grid Generation: Foundations and Applications,*Elsevier, Amsterdam.

Virieux, J., 1986. *P-SV* wave propagation in heterogeneous media: Velocity–stress finite-difference method, *Geophysics,* **51**, 889–901.

Wapenaar, C.P.A., Verschuur, D.J. & Hermann, P., 1992. Amplitude preprocessing of single and multicomponent seismic data, *Geophysics,* **57**, 1178–1188.

Zhang, J., 1997. Quadrangle-grid velocity–stress finite-difference method for elastic wave-propagation simulation, *Geophys. J. Int.,* **131**, 127–134.

Zhang, J. & Liu, S., 1997. Transmission boundary condition for mixed variable finite-difference method, *Acta Mechanica Solida Sinica,* **10**, 366–373.

Zhang, J. & Liu, T., 1999. *P-SV*-wave propagation in heterogeneous media: grid method, *Geophys. J. Int.,* **136**, 431–438.

Zienkiewicz, O.C. & Taylor, R.L., 1989. *The Finite Element Method,* 4th edn, McGraw-Hill, New York.

DISPERSION RELATION OF THE PARALLELEPIPED GRID METHOD

We assume a uniform infinite medium that supports a plane wave. Substituting eq. (11) into eq. (1) then into eq. (9) (together with eq. 3) provides a second-order system of difference equations in displacements only. This system can be written in matrix form using the second-order finite-difference operators D_{xx}, D_{yy}, D_{zz}, D_{xy}, D_{xz}, D_{yz} and D_{tt}:

$$\begin{bmatrix} \alpha^2 D_{xx} + \beta^2 D_{yy} + \beta^2 D_{zz} - D_{tt} & (\alpha^2 - \beta^2) D_{xy} & (\alpha^2 - \beta^2) D_{xz} \\ (\alpha^2 - \beta^2) D_{xy} & \beta^2 D_{xx} + \alpha^2 D_{yy} + \beta^2 D_{zz} - D_{tt} & (\alpha^2 - \beta^2) D_{yz} \\ (\alpha^2 - \beta^2) D_{xz} & (\alpha^2 - \beta^2) D_{yz} & \beta^2 D_{xx} + \beta^2 D_{yy} + \alpha^2 D_{zz} - D_{tt} \end{bmatrix} \begin{Bmatrix} u_1 \\ u_2 \\ u_3 \end{Bmatrix} = 0, \tag{A1}$$

where $\beta = \sqrt{\mu/\rho}$ is the *S*-wave velocity and $\alpha = \sqrt{(\lambda + 2\mu)/\rho}$ is the *P*-wave velocity. With $p^j_{l,m,n}$ denoting the field variable value at grid point (l, m, n) at time level j, the second-order finite-difference operators in eq. (A1) can be expressed as follows:

$$
\begin{aligned}
D_{xx}p^j_{l,m,n} &= \frac{1}{16\Delta x^2\Delta z^2\sin^2\theta}\left[(\Delta z-\Delta x\cos\theta)^2 p^j_A - 2(\Delta z^2-\Delta x^2\cos^2\theta)p^j_B + (\Delta z+\Delta x\cos\theta)^2 p^j_C\right]\\
D_{xy}p^j_{l,m,n} &= \frac{1}{16\Delta x\Delta y\Delta z\sin\theta}\left[(\Delta z-\Delta x\cos\theta)p^j_D - (\Delta z+\Delta x\cos\theta)p^j_E\right]\\
D_{xz}p^j_{l,m,n} &= \frac{1}{16\Delta x\Delta z^2\sin\theta}\left[(\Delta z-\Delta x\cos\theta)\left(p^j_A+p^j_B\right) - (\Delta z+\Delta x\cos\theta)\left(p^j_B+p^j_C\right)\right]\\
D_{yy}p^j_{l,m,n} &= \frac{1}{16\Delta y^2}\left[p^j_A+2p^j_B+p^j_C+4p^j_F\right]\\
D_{yz}p^j_{l,m,n} &= \frac{1}{16\Delta y\Delta z}\left[p^j_D+p^j_E\right]\\
D_{zz}p^j_{l,m,n} &= \frac{1}{16\Delta z^2}\left[p^j_A+2p^j_B+p^j_C\right]\\
D_{tt}p^j_{l,m,n} &= \frac{1}{\Delta t^2}\left[p^{j+1}_{l,m,n}+p^{j-1}_{l,m,n}-2p^j_{l,m,n}\right],
\end{aligned}
\tag{A2}
$$

where θ is the angle of one facet against the horizontal facet of the parallelepiped grids, Δx, Δy and Δz are the lengths of three sides of the parallelepiped grid, Δt is time sampling interval, and we have

$$
\begin{aligned}
p^j_A &= p^j_{l-1,m-1,n-1}+p^j_{l-1,m+1,n-1}+p^j_{l+1,m-1,n+1}+p^j_{l+1,m+1,n+1}+2p^j_{l-1,m,n-1}+2p^j_{l+1,m,n+1}-2p^j_{l,m-1,n}-2p^j_{l,m+1,n}-4p^j_{l,m,n}\\
p^j_B &= p^j_{l,m-1,n-1}+p^j_{l,m+1,n-1}+p^j_{l,m-1,n+1}+p^j_{l,m+1,n+1}+2p^j_{l,m,n-1}+2p^j_{l,m,n+1}-p^j_{l+1,m-1,n}-p^j_{l-1,m-1,n}-p^j_{l-1,m+1,n}-p^j_{l+1,m+1,n}\\
&\quad -2p^j_{l-1,m,n}-2p^j_{l+1,m,n}\\
p^j_C &= p^j_{l+1,m-1,n-1}+p^j_{l+1,m+1,n-1}+p^j_{l-1,m-1,n+1}+p^j_{l-1,m+1,n+1}+2p^j_{l+1,m,n-1}+2p^j_{l-1,m,n+1}-2p^j_{l,m-1,n}-2p^j_{l,m+1,n}-4p^j_{l,m,n}\\
p^j_D &= p^j_{l-1,m-1,n-1}+p^j_{l,m-1,n-1}+p^j_{l-1,m-1,n}+p^j_{l+1,m+1,n+1}+p^j_{l,m+1,n+1}+p^j_{l+1,m+1,n}-p^j_{l-1,m+1,n-1}-p^j_{l,m+1,n-1}-p^j_{l-1,m+1,n}\\
&\quad -p^j_{l+1,m-1,n+1}-p^j_{l,m-1,n+1}-p^j_{l+1,m-1,n}\\
p^j_E &= p^j_{l+1,m-1,n-1}+p^j_{l,m-1,n-1}+p^j_{l+1,m-1,n}+p^j_{l-1,m+1,n+1}+p^j_{l-1,m+1,n}+p^j_{l,m+1,n+1}-p^j_{l+1,m+1,n-1}-p^j_{l,m+1,n-1}-p^j_{l+1,m+1,n}\\
&\quad -p^j_{l-1,m-1,n+1}-p^j_{l-1,m-1,n}-p^j_{l,m-1,n+1}\\
p^j_F &= p^j_{l+1,m+1,n}+p^j_{l-1,m+1,n}+p^j_{l-1,m-1,n}+p^j_{l+1,m-1,n}+2p^j_{l,m+1,n}+2p^j_{l,m-1,n}-p^j_{l+1,m,n+1}-p^j_{l-1,m,n+1}-p^j_{l-1,m,n-1}\\
&\quad -p^j_{l+1,m,n-1}-2p^j_{l,m,n+1}-2p^j_{l,m,n-1}.
\end{aligned}
$$

Let the frequency of the plane wave be ω and the wavenumbers in the x, y and z directions be, respectively, k_x, k_y and k_z. The displacement vector at grid point (l, m, n) at time level j is

$$
\left\{(u_1)^j_{l,m,n}\quad (u_2)^j_{l,m,n}\quad (u_3)^j_{l,m,n}\right\}^{\mathrm{T}} = \{a\quad b\quad c\}^{\mathrm{T}}\exp[i(k_1 l+k_2 m+k_3 n-\omega j\Delta t)],
\tag{A3}
$$

where $\{a\ \ b\ \ c\}^{\mathrm{T}}$ is the displacement vector at (0, 0, 0) at the initial time level and $k_1=(k_x\sin\theta+k_z\cos\theta)\Delta x$, $k_2=k_y\Delta y$, $k_3=k_z\Delta z$. Substituting eq. (A3) into the finite-difference operators of eq. (A2) and then substituting them into eq. (A1), we transform the coefficient matrix of eq. (A1) into a new one where the operators D_{xx}, D_{yy}, D_{zz}, D_{xy}, D_{xz}, D_{yz} and D_{tt} are replaced by follows:

$$
\begin{aligned}
D_{xx} &= -\frac{4}{\Delta x^2\Delta z^2\sin^2\theta}\cos^2(k_2/2)[\Delta z\sin(k_1/2)\cos(k_3/2)-\Delta x\cos\theta\cos(k_1/2)\sin(k_3/2)]^2,\\
D_{xy} &= -\frac{2}{\Delta x\Delta y\Delta z\sin\theta}\sin(k_2)\cos(k_1/2)\cos(k_3/2)[\Delta z\sin(k_1/2)\cos(k_3/2)-\Delta x\cos\theta\cos(k_1/2)\sin(k_3/2)],\\
D_{xz} &= -\frac{4}{\Delta x\Delta z^2\sin\theta}\cos^2(k_2/2)\cos(k_1/2)\sin(k_3/2)[\Delta z\sin(k_1/2)\cos(k_3/2)-\Delta x\cos\theta\cos(k_1/2)\sin(k_3/2)]^2,\\
D_{yy} &= -\frac{4}{\Delta y^2}\cos^2(k_1/2)\sin^2(k_2/2)\cos^2(k_3/2),\quad D_{yz} = -\frac{1}{\Delta y\Delta z}\cos^2(k_1/2)\sin(k_2)\sin(k_3),\\
D_{zz} &= -\frac{4}{\Delta z^2}\cos^2(k_1/2)\cos^2(k_2/2)\sin^2(k_3/2),\quad D_{tt} = \frac{4}{\Delta t^2}\sin^2[(\omega\Delta t)/2].
\end{aligned}
$$

It should be noted that there should be a non-zero solution for the vector $\{a\ \ b\ \ c\}^{\mathrm{T}}$. Hence, the new coefficient matrix should be singular. Letting the norm of the matrix be zero gives the dispersion relation as

$$
\begin{aligned}
\sin^2\left(\frac{\omega\Delta t}{2}\right) = V^2\Delta t^2\Bigg\{&\frac{1}{\Delta x^2\Delta z^2\sin^2\theta}\cos^2(k_2/2)[\Delta z\sin(k_1/2)\cos(k_3/2)-\Delta x\cos\theta\cos(k_1/2)\sin(k_3/2)]^2\\
&+\frac{1}{\Delta y^2}\cos^2(k_1/2)\sin^2(k_2/2)\cos^2(k_3/2)+\frac{1}{\Delta z^2}\cos^2(k_1/2)\cos^2(k_2/2)\sin^2(k_3/2)\Bigg\}.
\end{aligned}
\tag{A4}
$$

Eq. (A4) denotes the P-wave dispersion relation when V is the P-wave velocity, and the S-wave dispersion relation when V is the S-wave velocity.

DISPERSION RELATIONS OF THE TETRAHEDRAL GRID METHOD

We discuss a case when the tetrahedral grids are generated through splitting each right cube into five tetrahedrons of a regular orthogonal mesh. This inhomogeneous tetrahedral mesh makes the dispersion relations very complex. For simplicity, we assume the infinite medium with a Poisson ratio of 0.25, i.e. $\lambda = \mu$. By substituting eq. (10) into eq. (1) then into eq. (9) (together with eq. 3), the finite-difference equations for the tetrahedral grid method can be obtained as

$$\begin{aligned}
&\frac{1}{\Delta t^2}\left[(u_1)^{j+1}_{l,m,n} + (u_1)^{j-1}_{l,m,n} - 2(u_1)^{j}_{l,m,n}\right] = \alpha_1(u_1)^{j}_{l,m,n} + \alpha_2(u_1)^{j}_{l+1,m,n} + \alpha_2(u_1)^{j}_{l-1,m,n} + \alpha_3(u_1)^{j}_{l,m+1,n} + \alpha_3(u_1)^{j}_{l,m-1,n} + \alpha_3(u_1)^{j}_{l,m,n+1}\\
&\quad + \alpha_3(u_1)^{j}_{l,m,n-1} + \alpha_4(u_1)^{j}_{l+1,m+1,n} + \alpha_4(u_1)^{j}_{l-1,m-1,n} + \alpha_4(u_1)^{j}_{l+1,m,n+1} + \alpha_4(u_1)^{j}_{l-1,m,n-1} + \alpha_4(u_1)^{j}_{l-1,m+1,n} + \alpha_4(u_1)^{j}_{l+1,m-1,n}\\
&\quad + \alpha_4(u_1)^{j}_{l-1,m,n+1} + \alpha_4(u_1)^{j}_{l+1,m,n-1} + \alpha_5(u_1)^{j}_{l,m+1,n+1} + \alpha_5(u_1)^{j}_{l,m-1,n-1} + \alpha_5(u_1)^{j}_{l,m-1,n+1} + \alpha_5(u_1)^{j}_{l,m+1,n-1} + \alpha_6(u_2)^{j}_{l+1,m+1,n}\\
&\quad + \alpha_6(u_2)^{j}_{l-1,m-1,n} - \alpha_6(u_2)^{j}_{l-1,m+1,n} - \alpha_6(u_2)^{j}_{l+1,m-1,n} + \alpha_7(u_2)^{j}_{l+1,m,n+1} + \alpha_7(u_2)^{j}_{l-1,m,n+1} + \alpha_7(u_2)^{j}_{l,m+1,n-1} + \alpha_7(u_2)^{j}_{l,m-1,n-1}\\
&\quad - \alpha_7(u_2)^{j}_{l,m+1,n+1} - \alpha_7(u_2)^{j}_{l,m-1,n+1} - \alpha_7(u_2)^{j}_{l+1,m,n-1} - \alpha_7(u_2)^{j}_{l-1,m,n-1} + \alpha_6(u_3)^{j}_{l+1,m,n+1} + \alpha_6(u_3)^{j}_{l-1,m,n-1} - \alpha_6(u_3)^{j}_{l-1,m,n+1}\\
&\quad - \alpha_6(u_3)^{j}_{l+1,m,n-1} + \alpha_7(u_3)^{j}_{l+1,m+1,n} + \alpha_7(u_3)^{j}_{l-1,m+1,n} + \alpha_7(u_3)^{j}_{l,m-1,n+1} + \alpha_7(u_3)^{j}_{l,m-1,n-1} - \alpha_7(u_3)^{j}_{l,m+1,n+1} - \alpha_7(u_3)^{j}_{l,m+1,n-1}\\
&\quad - \alpha_7(u_3)^{j}_{l-1,m-1,n} - \alpha_7(u_3)^{j}_{l+1,m-1,n}
\end{aligned} \tag{B1}$$

$$\begin{aligned}
&\frac{1}{\Delta t^2}\left[(u_2)^{j+1}_{l,m,n} + (u_2)^{j-1}_{l,m,n} - 2(u_2)^{j}_{l,m,n}\right] = \alpha_1(u_2)^{j}_{l,m,n} + \alpha_2(u_2)^{j}_{l,m+1,n} + \alpha_2(u_2)^{j}_{l,m-1,n} + \alpha_3(u_2)^{j}_{l+1,m,n} + \alpha_3(u_2)^{j}_{l-1,m,n} + \alpha_3(u_2)^{j}_{l,m,n+1}\\
&\quad + \alpha_3(u_2)^{j}_{l,m,n-1} + \alpha_4(u_2)^{j}_{l+1,m+1,n} + \alpha_4(u_2)^{j}_{l-1,m-1,n} + \alpha_4(u_2)^{j}_{l,m+1,n+1} + \alpha_4(u_2)^{j}_{l,m-1,n-1} + \alpha_4(u_2)^{j}_{l-1,m+1,n} + \alpha_4(u_2)^{j}_{l+1,m-1,n}\\
&\quad + \alpha_4(u_2)^{j}_{l,m-1,n+1} + \alpha_4(u_2)^{j}_{l,m+1,n-1} + \alpha_5(u_2)^{j}_{l+1,m,n+1} + \alpha_5(u_2)^{j}_{l-1,m,n-1} + \alpha_5(u_2)^{j}_{l-1,m,n+1} + \alpha_5(u_2)^{j}_{l+1,m,n-1} + \alpha_6(u_1)^{j}_{l+1,m+1,n}\\
&\quad + \alpha_6(u_1)^{j}_{l-1,m-1,n} - \alpha_6(u_1)^{j}_{l-1,m+1,n} - \alpha_6(u_1)^{j}_{l+1,m-1,n} + \alpha_7(u_1)^{j}_{l,m+1,n+1} + \alpha_7(u_1)^{j}_{l,m-1,n+1} + \alpha_7(u_1)^{j}_{l+1,m,n-1} + \alpha_7(u_1)^{j}_{l-1,m,n-1}\\
&\quad - \alpha_7(u_1)^{j}_{l+1,m,n+1} - \alpha_7(u_1)^{j}_{l-1,m,n+1} - \alpha_7(u_1)^{j}_{l,m+1,n-1} - \alpha_7(u_1)^{j}_{l,m-1,n-1} + \alpha_6(u_3)^{j}_{l,m+1,n+1} + \alpha_6(u_3)^{j}_{l,m-1,n-1} - \alpha_6(u_3)^{j}_{l,m-1,n+1}\\
&\quad - \alpha_6(u_3)^{j}_{l,m+1,n-1} + \alpha_7(u_3)^{j}_{l+1,m+1,n} + \alpha_7(u_3)^{j}_{l+1,m-1,n} + \alpha_7(u_3)^{j}_{l-1,m,n+1} + \alpha_7(u_3)^{j}_{l-1,m,n-1} - \alpha_7(u_3)^{j}_{l+1,m,n+1} - \alpha_7(u_3)^{j}_{l+1,m,n-1}\\
&\quad - \alpha_7(u_3)^{j}_{l-1,m+1,n} - \alpha_7(u_3)^{j}_{l-1,m-1,n}
\end{aligned} \tag{B2}$$

$$\begin{aligned}
&\frac{1}{\Delta t^2}\left[(u_3)^{j+1}_{l,m,n} + (u_3)^{j-1}_{l,m,n} - 2(u_3)^{j}_{l,m,n}\right] = \alpha_1(u_3)^{j}_{l,m,n} + \alpha_2(u_3)^{j}_{l,m,n+1} + \alpha_2(u_3)^{j}_{l,m,n-1} + \alpha_3(u_3)^{j}_{l+1,m,n} + \alpha_3(u_3)^{j}_{l-1,m,n} + \alpha_3(u_3)^{j}_{l,m+1,n}\\
&\quad + \alpha_3(u_3)^{j}_{l,m-1,n} + \alpha_4(u_3)^{j}_{l+1,m,n+1} + \alpha_4(u_3)^{j}_{l-1,m,n-1} + \alpha_4(u_3)^{j}_{l,m+1,n+1} + \alpha_4(u_3)^{j}_{l,m-1,n-1} + \alpha_4(u_3)^{j}_{l,m-1,n+1} + \alpha_4(u_3)^{j}_{l,m+1,n-1}\\
&\quad + \alpha_4(u_3)^{j}_{l-1,m,n+1} + \alpha_4(u_3)^{j}_{l+1,m,n-1} + \alpha_5(u_3)^{j}_{l+1,m+1,n} + \alpha_5(u_3)^{j}_{l-1,m-1,n} + \alpha_5(u_3)^{j}_{l-1,m+1,n} + \alpha_5(u_3)^{j}_{l+1,m-1,n} + \alpha_6(u_1)^{j}_{l+1,m,n+1}\\
&\quad + \alpha_6(u_1)^{j}_{l-1,m,n-1} - \alpha_6(u_1)^{j}_{l-1,m,n+1} - \alpha_6(u_1)^{j}_{l+1,m,n-1} + \alpha_7(u_1)^{j}_{l,m+1,n+1} + \alpha_7(u_1)^{j}_{l,m+1,n-1} + \alpha_7(u_1)^{j}_{l-1,m-1,n} + \alpha_7(u_1)^{j}_{l+1,m-1,n}\\
&\quad - \alpha_7(u_1)^{j}_{l+1,m+1,n} - \alpha_7(u_1)^{j}_{l-1,m+1,n} - \alpha_7(u_1)^{j}_{l,m-1,n+1} - \alpha_7(u_1)^{j}_{l,m-1,n-1} + \alpha_6(u_2)^{j}_{l,m+1,n+1} + \alpha_6(u_2)^{j}_{l,m-1,n-1} - \alpha_6(u_2)^{j}_{l,m-1,n+1}\\
&\quad - \alpha_6(u_2)^{j}_{l,m+1,n-1} + \alpha_7(u_2)^{j}_{l+1,m,n+1} + \alpha_7(u_2)^{j}_{l+1,m,n-1} + \alpha_7(u_2)^{j}_{l-1,m+1,n} + \alpha_7(u_2)^{j}_{l-1,m-1,n} - \alpha_7(u_2)^{j}_{l+1,m+1,n} - \alpha_7(u_2)^{j}_{l+1,m-1,n}\\
&\quad - \alpha_7(u_2)^{j}_{l-1,m,n+1} - \alpha_7(u_2)^{j}_{l-1,m,n-1},
\end{aligned} \tag{B3}$$

where $(u_i)^{j}_{l,m,n}$, for $i = 1, \ldots, 3$, denote the displacement components at grid point (l, m, n) at time level j, Δt is time sampling interval, and we have

$$\alpha_1 = -\frac{5}{3h^2}(\alpha^2 + 2\beta^2), \quad \alpha_2 = \frac{2\alpha^2}{3h^2}, \quad \alpha_3 = \frac{2\beta^2}{3h^2}, \quad \alpha_4 = \frac{\alpha^2}{12h^2}, \quad \alpha_5 = \frac{1}{12h^2}(2\beta^2 - \alpha^2), \quad \alpha_6 = \frac{1}{4h^2}(\alpha^2 - \beta^2),$$
$$\alpha_7 = \frac{1}{12h^2}(3\beta^2 - \alpha^2).$$

Here h is the interval of the regular orthogonal mesh, α and β are the *P*- and *S*-wave velocities, respectively.

Assuming a uniform infinite medium that supports a plane wave with a frequency of ω, the displacement components at the nodes can be expressed as

$$\left\{(u_1)^{j}_{l,m,n} \quad (u_2)^{j}_{l,m,n} \quad (u_3)^{j}_{l,m,n}\right\}^{\mathrm{T}} = \{a \quad b \quad c\}^{\mathrm{T}} \exp[i(lhk_x + mhk_y + nhk_z - \omega j\Delta t)], \tag{B4}$$

where k_x, k_y and k_z are the wavenumbers in the x, y and z directions, $\{a \;\; b \;\; c\}^{\mathrm{T}}$ is the displacement vector at (0, 0, 0) at the initial time level. Let $\upsilon = 0.25$. Substituting eq. (B4) into eqs (B1)–(B3) gives the following:

$$\begin{bmatrix}
16\cos(k_x h) + s_1 + 6s_2 + 6s_4 - 2s_3 + s_0 & s_5 & s_7\\
s_5 & 16\cos(k_y h) + s_1 + 6s_2 + 6s_3 - 2s_4 + s_0 & s_6\\
s_7 & s_6 & 16\cos(k_z h) + s_1 + 6s_3 + 6s_4 - 2s_2 + s_0
\end{bmatrix}
\begin{Bmatrix} a \\ b \\ c \end{Bmatrix} = 0, \tag{B5}$$

where

$s_1 = 8\cos(k_x h) + 8\cos(k_y h) + 8\cos(k_z h) - 50, \quad s_2 = \cos(k_x h)\cos(k_y h), \quad s_3 = \cos(k_y h)\cos(k_z h),$

$s_4 = \cos(k_x h)\cos(k_z h), \quad s_5 = -12\sin(k_x h)\sin(k_y h), \quad s_6 = -12\sin(k_y h)\sin(k_z h), \quad s_7 = -12\sin(k_x h)\sin(k_z h),$

$$s_0 = \frac{72h^2}{\Delta t^2\alpha^2}\sin^2\left(\frac{\omega\Delta t}{2}\right).$$

It is noted that there should be a non-zero solution for the vector $\{a \;\; b \;\; c\}^{\mathrm{T}}$ in eq. (B5). Hence, the matrix in eq. (B5) must be singular. Substituting s_0, etc. into the coefficient matrix of eq. (B5) and letting the norm of the matrix be zero, we can obtain the dispersion relations for the tetrahedral grid method. These dispersion relations are very complicated. For a special case, that is $k_x = k_y = k_z = k$, we have a simple form as follows:

$$\frac{72h^2}{\Delta t^2\alpha^2}\sin^2\left(\frac{\omega\Delta t}{2}\right) = 74 - 34\cos^2(kh) - 40\cos(kh) \tag{B6}$$

$$\frac{24h^2}{\Delta t^2\beta^2}\sin^2\left(\frac{\omega\Delta t}{2}\right) = 38 + 2\cos^2(kh) - 40\cos(kh). \tag{B7}$$

Eq. (B7) are two equal roots of the zero-norm of the matrix of eq. (B5), which denotes the *S*-wave dispersion relation; and eq. (B6) denotes the *P*-wave dispersion relation.

FINITE-DIFFERENCE EQUATIONS FOR THE SURFACE

With $(u_i)^j_{l,m,n}$, for $i = 1, \ldots, 3$, denoting the displacement components at grid point (l, m, n) at time level j, the finite-difference equations for the surface can be expressed as

$$\begin{aligned}
&\frac{1}{\Delta t^2}\left[(u_1)^{j+1}_{l,m,1} + (u_1)^{j-1}_{l,m,1} - 2(u_1)^j_{l,m,1}\right] = \alpha_1(u_1)^j_{l,m,1} + \alpha_2(u_1)^j_{l+1,m,1} + \alpha_2(u_1)^j_{l-1,m,1} + \alpha_3(u_1)^j_{l,m-1,1} + \alpha_3(u_1)^j_{l,m+1,1} + \alpha_4(u_1)^j_{l,m,2}\\
&+\alpha_5(u_1)^j_{l-1,m-1,1} + \alpha_5(u_1)^j_{l+1,m+1,1} + \alpha_5(u_1)^j_{l-1,m,2} + \alpha_5(u_1)^j_{l+1,m,2} + \alpha_6(u_1)^j_{l,m-1,2} + \alpha_6(u_1)^j_{l,m+1,2} - \alpha_7(u_2)^j_{l,m,1} + \alpha_7(u_2)^j_{l+1,m,1}\\
&+\alpha_7(u_2)^j_{l-1,m,1} + \alpha_7(u_2)^j_{l,m-1,1} + \alpha_7(u_2)^j_{l,m+1,1} - \alpha_8(u_2)^j_{l-1,m-1,1} - \alpha_8(u_2)^j_{l+1,m+1,1} + \alpha_9(u_2)^j_{l-1,m,2} + \alpha_9(u_2)^j_{l+1,m,2} - \alpha_9(u_2)^j_{l,m-1,2}\\
&-\alpha_9(u_2)^j_{l,m+1,2} + \alpha_{10}(u_3)^j_{l+1,m,1} - \alpha_{10}(u_3)^j_{l-1,m,1} + \alpha_{11}(u_3)^j_{l-1,m,2} - \alpha_{11}(u_3)^j_{l+1,m,2} - \alpha_{12}(u_3)^j_{l-1,m-1,1} + \alpha_{12}(u_3)^j_{l+1,m+1,1}\\
&+\alpha_{12}(u_3)^j_{l,m-1,2} - \alpha_{12}(u_3)^j_{l,m+1,2}
\end{aligned} \tag{C1}$$

$$\begin{aligned}
&\frac{1}{\Delta t^2}\left[(u_2)^{j+1}_{l,m,1} + (u_2)^{j-1}_{l,m,1} - 2(u_2)^j_{l,m,1}\right] = \alpha_1(u_2)^j_{l,m,1} + \alpha_2(u_2)^j_{l,m-1,1} + \alpha_2(u_2)^j_{l,m+1,1} + \alpha_3(u_2)^j_{l+1,m,1} + \alpha_3(u_2)^j_{l-1,m,1} + \alpha_4(u_2)^j_{l,m,2}\\
&+\alpha_5(u_2)^j_{l-1,m-1,1} + \alpha_5(u_2)^j_{l+1,m+1,1} + \alpha_5(u_2)^j_{l,m-1,2} + \alpha_5(u_2)^j_{l,m+1,2} + \alpha_6(u_2)^j_{l-1,m,2} + \alpha_6(u_2)^j_{l+1,m,2} - \alpha_7(u_1)^j_{l,m,1} + \alpha_7(u_1)^j_{l+1,m,1}\\
&+\alpha_7(u_1)^j_{l-1,m,1} + \alpha_7(u_1)^j_{l,m-1,1} + \alpha_7(u_1)^j_{l,m+1,1} - \alpha_8(u_1)^j_{l-1,m-1,1} - \alpha_8(u_1)^j_{l+1,m+1,1} + \alpha_9(u_1)^j_{l,m-1,2} + \alpha_9(u_1)^j_{l,m+1,2} - \alpha_9(u_1)^j_{l-1,m,2}\\
&-\alpha_9(u_1)^j_{l+1,m,2} + \alpha_{10}(u_3)^j_{l,m-1,1} - \alpha_{10}(u_3)^j_{l,m+1,1} + \alpha_{11}(u_3)^j_{l,m+1,2} - \alpha_{11}(u_3)^j_{l,m-1,2} + \alpha_{12}(u_3)^j_{l-1,m-1,1} - \alpha_{12}(u_3)^j_{l+1,m+1,1}\\
&-\alpha_{12}(u_3)^j_{l-1,m,2} + \alpha_{12}(u_3)^j_{l+1,m,2}
\end{aligned} \tag{C2}$$

$$\begin{aligned}
&\frac{1}{\Delta t^2}\left[(u_3)^{j+1}_{l,m,1} + (u_3)^{j-1}_{l,m,1} - 2(u_3)^j_{l,m,1}\right] = \alpha_1(u_3)^j_{l,m,1} + \alpha_{13}(u_3)^j_{l,m,2} + \alpha_3(u_3)^j_{l+1,m,1} + \alpha_3(u_3)^j_{l-1,m,1} + \alpha_3(u_3)^j_{l,m-1,1} + \alpha_3(u_3)^j_{l,m+1,1}\\
&+\alpha_5(u_3)^j_{l-1,m,2} + \alpha_5(u_3)^j_{l+1,m,2} + \alpha_5(u_3)^j_{l,m-1,2} + \alpha_5(u_3)^j_{l,m+1,2} + \alpha_6(u_3)^j_{l-1,m-1,1} + \alpha_6(u_3)^j_{l+1,m+1,1} - \alpha_{10}(u_1)^j_{l+1,m,1} + \alpha_{10}(u_1)^j_{l-1,m,1}\\
&+\alpha_8(u_1)^j_{l-1,m,2} - \alpha_8(u_1)^j_{l+1,m,2} + \alpha_9(u_1)^j_{l-1,m-1,1} - \alpha_9(u_1)^j_{l+1,m+1,1} - \alpha_9(u_1)^j_{l,m-1,2} + \alpha_9(u_1)^j_{l,m+1,2} - \alpha_{10}(u_2)^j_{l,m-1,1} + \alpha_{10}(u_2)^j_{l,m+1,1}\\
&-\alpha_{11}(u_2)^j_{l,m-1,2} + \alpha_{11}(u_2)^j_{l,m+1,2} - \alpha_{12}(u_2)^j_{l-1,m-1,1} + \alpha_{12}(u_2)^j_{l+1,m+1,1} + \alpha_{12}(u_2)^j_{l-1,m,2} - \alpha_{12}(u_2)^j_{l+1,m,2},
\end{aligned} \tag{C3}$$

where Δt is time sampling interval, and we have

$$\alpha_1 = -\frac{5}{3h^2}(\alpha^2 + 2\beta^2), \quad \alpha_2 = \frac{2\alpha^2}{3h^2}, \quad \alpha_3 = \frac{2\beta^2}{3h^2}, \quad \alpha_4 = \frac{4\beta^2}{3h^2}, \quad \alpha_5 = \frac{\alpha^2}{6h^2}, \quad \alpha_6 = \frac{1}{6h^2}(2\beta^2 - \alpha^2),$$

$$\alpha_7 = \frac{1}{3h^2}(\alpha^2 - \beta^2), \quad \alpha_8 = \frac{1}{2h^2}(\alpha^2 - \beta^2), \quad \alpha_9 = \frac{1}{6h^2}(\alpha^2 - 3\beta^2), \quad \alpha_{10} = \frac{1}{3h^2}(\alpha^2 - 3\beta^2), \quad \alpha_{11} = \alpha_8,$$

$$\alpha_{12} = \frac{1}{6h^2}(\alpha^2 - 3\beta^2), \quad \alpha_{13} = \frac{4\alpha^2}{3h^2}.$$

Here h is the interval of the regular orthogonal mesh, α and β are the *P*- and *S*-wave velocities, respectively.